Global representation of tropical cyclone-induced ocean thermal changes using Argo data

Lijing Cheng[1], Jiang Zhu[1*], Ryan L. Sriver[2]

[1] International Center for Climate and Environment Sciences, Institute of Atmospheric Physics, Chinese Academy of Sciences, Beijing, China;

[2] Department of Atmospheric Sciences, University of Illinois, Urbana-Champaign, IL, USA

Correspondence to: J. Zhu (jzhu@mail.iap.ac.cn)

Abstract

Argo floats are used to examine tropical cyclone (TC)-induced ocean thermal changes on the global scale by comparing temperature profiles before and after TC passage. We present a footprint method that analyzes cross-track thermal responses along all storm tracks during the period 2004-2012. We combine the results into composite representations of the vertical structure of the average thermal response for two different categories: tropical storms/depressions (TS/TD) and hurricanes. The two footprint composites are functions of three variables: cross-track distance, water depth and time relative to TC passage. We find that this footprint strategy captures the major features of the upper-ocean thermal response to TCs on time scales up to 20 days when compared against previous case study results using in situ measurements. On the global scale, TCs are responsible for 1.87 PW (11.05 W/m^2) of heat transfer annually from the global ocean to the atmosphere during storm passage (0-3 days). Of this total, 1.05±0.20 PW (4.80±0.85 W/m^2) is caused by Tropical storms/Tropical depressions (TS/TD) and 0.82±0.21 PW (6.25±1.5 W/m^2) is caused by hurricanes. Our findings indicate that ocean heat loss by TCs may be a substantial missing piece of the global ocean heat budget. Net changes in OHC after storm passage is estimated by analyzing the temperature anomalies during wake recovery following storm events (4-20 days after storm passage) relative to pre-storm conditions. Results indicate the global ocean experiences a 0.75±0.25 PW (5.98±2.1 W/m^2) net heat gain annually for hurricanes. In contrast, under TS/TD conditions, the ocean experiences 0.41±0.21 PW

(1.90±0.96 W/m^2) net ocean heat loss, suggesting the overall oceanic thermal response is particularly sensitive to the intensity of the event. The net ocean heat uptake caused by all storms is 0.34 PW.

1 Introduction

Tropical cyclones (TCs) provide an effective mechanism to transport heat, mass and nutrients in the ocean, while also exchanging enthalpy with the atmosphere. Multiple lines of evidence from previous observational and modeling studies indicate that these relatively small scale and transient events can influence large scale dynamical processes in both the ocean (Emanuel, 2001; Sriver and Huber, 2007) and atmosphere (Camargo and Sobel, 2005; Hart, 2011; Jansen et al. 2010; Sriver and Huber, 2010)

TCs affect ocean processes and properties on multiple spatial and temporal scales. On scales relevant for climate dynamics, the cumulative effects of TCs on the ocean have been shown to be important for controlling tropical and subtropical ocean temperature patterns through enhanced subsurface mixing (Fedorov et al., 2010; Sriver et al., 2010). It has been hypothesized that increases in this mixing associated with more TC activity is capable of sustaining climates with permanent El Nino-like temperature patterns such as during the early Pliocene, ~5 million years ago (Fedorov et al., 2010). On inter-seasonal scales, TC-induced changes in ocean temperature can impact the atmospheric circulations through dynamical connections affecting mid-latitude weather in subsequent winters (Hart, 2011; Hart et al., 2007b). This mechanism, and in general the relatively strong thermal inertia of the ocean, implies a longer memory of tropical cyclones in the ocean than in the atmosphere. On synoptic scales, TC-induced cooling at the surface via enhanced mixing can limit TC intensification (e.g. Ginis, 2002).

Understanding the ocean's response to TCs on various spatial and temporal scales is an ongoing area of active research. Since the 1950s, ocean vessels, moorings, and aircraft have been observing ocean conditions in TC-affected regions, which has assisted in building the basic framework for understanding how the ocean responds to TC forcing (Black and Dickey, 2008; Price, 1981, 1983; Price et al., 1994; Shay and Elsberry, 1987; Shay et al., 1989). The response of the upper ocean to TC forcing is typically characterized by surface cooling in the storm wake and subsurface warming

caused by a variety of oceanic and atmospheric processes, including generation of near-inertial internal oscillations, geostrophic advection, Ekman pumping, and surface fluxes. Previous studies analyzing the ocean response to TCs have generally been limited by the availability of observations and/or focus on a limited number of storms, resulting in storm-to-storm variations (Bell et al., 2012; Cione and Uhlhorn, 2003; Lin et al., 2009a; Lin et al., 2009b). Until recently, these limitations in data coverage have prevented a global-scale perspective of how TCs affect the ocean.

Previous efforts to quantify the impact of TCs on upper OHC have relied primarily on near-surface observations (Sriver and Huber, 2007; Sriver et al., 2008; Jansen et al., 2010) and Altimetry sea level data (Mei et al., 2013), inferring a redistribution of heat via vertical mixing. Because there is a relatively firm theoretical understanding of the ocean's response to TC wind forcing (Price, 1981), global SST fields from satellites and reanalysis serve as the basis for first-order estimates of TC impacts, because they offer global coverage and relatively high spatial and temporal resolution. But these methods come along with fundamental assumptions about the interior ocean response. For example, (Sriver and Huber, 2007) assume that the upper 50 m depth ocean is cooled homogeneously within TC cold wakes reflecting the temperature change observed at the surface, and all cooling is achieved through vertical mixing. Given these assumptions, they estimate 0.2-0.4 PW of heat is transported into the ocean interior globally. Using improved methodologies, several additional observational studies have generally supported this result (Jansen et al., 2010; Sriver et al., 2008; Mei et al., 2013).

A key uncertainty missing in the above studies is the effect of enthalpy exchange at the air-sea interface (Emanuel, 1991, 1999). Typically these fluxes are estimated by measuring the humidity near the sea surface using mooring instruments, and calculating the latent heat flux according to a parameterized bulk equation. A so-called drag coefficient is needed to approximate the efficiency of heat transfer, which is one of the sources of uncertainties in the high-wind weather conditions (Powell et al., 2003). Another source of uncertainty arises due to the spatial and temporal variations in humidity, temperature and wind speed under highly chaotic wind conditions, since the winds undergo rapid changes in direction and magnitude in TC conditions (Wright et al., 2001). Additionally, the effect of sea spray must also been taken into account, since it represents an efficient mechanism transporting

enthalpy in the air-sea boundary layer under strong winds. These uncertainties make the direct measurements of the air-sea fluxes difficult, and thus it is perhaps necessary to accumulate large numbers of measurements to achieve statistically significant results. Despite these limitations, studies have shown the air-sea heat fluxes within TCs are on the order of 2 to 3 times greater than the background heat fluxes in quiescent conditions (D'Asaro, 2003; Lin et al., 2009). These studies improve the understanding of the air-sea heat exchange by TCs, but global scale estimates are difficult.

Following the wind-drag based methodology, Trenberth and Fasullo (2007) use a high resolution model to examine the TC-induced water and energy budgets on the global scale. Their estimate of heat flux is based on an empirical relationship between heat flux and wind speed (Trenberth et al., 2007). They find that 0.17 PW heat is released from ocean to atmosphere within 400 km of the storm center and 0.58 PW within 1600 km.

These previous studies suggest that TCs induce a substantial amount of heat exchange between the atmosphere, oceanic mixed layer, and upper thermocline, thus these events may play an important role in influencing global heat budgets and climate. However, comprehensive global estimates of air-sea exchanges, ocean interior thermal changes, and net effects on OHC have not yet been estimated using global, vertically resolved ocean observations.

A key difficulty in quantifying the global distribution of TC-induced oceanic thermal response is the lack of all-weather observations with sufficient horizontal, vertical and temporal coverage and resolution. Since the year 2000, Argo profiling floats have provided a global network of *in-situ* ocean surface and subsurface observations (von Schuckmann and Le Traon, 2011; Willis et al., 2009). The profiles measure water temperature and salinity from the surface (~5m) to ~2000m depth, even under extreme weather conditions such as TCs. Since 2004, the Argo system has maintained a global array network with resolution of about 3 by 3 degrees in space similar to the XBT-based system (Freeland, 2009). However, the main advantage of the Argo system over previous observational systems is that the floats are more evenly distributed in space and time over the ocean and can observe conditions from greater depths.

Several recent studies have used Argo data to examine ocean conditions under TCs (Lin et al., 2009b; Liu et al., 2007; Mei et al., 2013; Park et al., 2011). Liu et al., (2007) concentrated on northwestern Pacific typhoons, suggesting that TC signals (e.g. sea surface cooling) can be captured by Argo data and these signals are statistically significant. Lin et al., (2009) examined ocean responses under a specific TC (Nargis), showing a clear ocean thermal change from a series of Argo data near the storm. These results support the reliability of Argo observations in severe weather conditions. More recent work examining TC-induced ocean heat content changes in the western Pacific (Park et al., 2011) represents the first attempt to investigate systematically the TC-induced ocean thermal changes on a basin-scale using Argo data. While the authors do identify a TC signature in the Argo data, the TC-induced subsurface temperature response is sensitive to the season in which TCs occur. Furthermore, the TC-induced effect is difficult to separate from the background variability, particularly for weak storms.

Here we present a new method to examine global TC-ocean interactions using Argo data, which examines all storms globally and characterizes the global mean of the cross-track ocean response to TCs using a footprint method that follows along the storm tracks. We categorize the TC events into two separate groups: Tropical storms/depressions (TS/TD) and Hurricanes. In addition, we separate the ocean's response into two stages: the forced stage (0-3 days relative to storm passage) and the recovery stage (4-20 days relative to storm passage). We use this technique to analyze TC-induced ocean thermal responses and latent heat fluxes on a global scale, accounting for regional variability in background ocean conditions. The paper is organized as follows. We describe the data and footprint methodology in section 2. We present the results and discussion in section 3. We discuss the caveats of the method in section 4, and section 5 outlines the main conclusions.

2 Data and Methods

2.1 Data

Argo floats drift freely at a fixed pressure (usually 1000 meters depth and occasionally at 1200m and 1500m) for about 9-10 days. After this period, the floats descend rapidly to a profiling pressure (usually 2000 meters deep) and then rise, collecting near-instantaneous profiles of pressure, temperature, and salinity data on their way to the surface (within a span of about 2 hours). The floats remain at the surface for less than one day, transmitting the data collected via a satellite link back to a ground station and allowing the satellite to determine their surface positions. The floats then sink again to a parking depth of ~1000 meters and repeat the cycle.

Argo data are available on the website of National Oceanographic Data Center/Global Argo Data Repository. In this study, we use Argo data from January 2004 to December 2012 (downloaded on October 2012). We discard all the profiles in the so-called grey list (Willis et al., 2009). Both delayed mode (data available several months after passing careful quality control processes) and real-time mode (data available to users within two days timeframe) data are used where available, and Argo quality control flags are used to eliminate spurious measurements. We apply an additional 'Boundary Check' as follows. If a temperature anomaly within 200m-1000m from a pair (discussed in more detail in section 2.2) is larger than 2^{o}C (or smaller than -2^{o}C), the anomaly is labeled as 'spurious'. If there are more than 5 'spurious' labels from a single pair, the pair is rejected and all of the 'spurious' anomalies are removed. This is a widely used quality control process and helps to get rid of the spikes and anomalous profiles.

Tropical cyclone information comes from the NOAA's Tropical Prediction Center 'best track' dataset (http://weather.unisys.com/). The data set contains 6-hourly records of maximum wind speeds, pressure and location. We collect all TC tracks globally between January 2004 to December 2012, totaling 885 events.

2.2 Composite footprint method

We introduce a footprint method that averages all of the TC-induced cross-track (i.e. perpendicular to the storm's direction of motion) ocean temperature changes. Argo

pairs are selected to compare temperature profiles before and after storm passage according to the following criteria:

1) The pre-storm Argo profile is within -12 to -2 days before storm passage and the post-storm Argo profile is within 0 to 20 days after storm passage. The 20-day limit is selected because SST changes are largely restored to pre-storm condition within 20 days after storm passage. Furthermore, it is increasingly difficult to separate TC effects from the seasonal cycle of SST on timescales longer than 20 days. Data within -2 to 0 days prior to storm passage are not used as pre-storm reference profiles, since they may be affected by TC processes (e.g. increased heat fluxes ahead of storms) and horizontal advection (Huang et al., 2009).

2) The locations of the pre-storm and post-storm Argo profiles are within 0.2 degrees of each other. Ideally, this comparison should be made at the same location, but it is not possible due to the heterogeneity of the observing system (both in space and time). Therefore, 0.2 degree is selected as the maximum horizontal distance between the reference and TC-affected Argo floats, since we believe it can both minimize the influences of the background signals (such as meso-scale eddies, boundary currents, and waves) and maximize the size of our TC-affected pairs dataset. Sensitivity analysis shows that the background ocean variability (not due directly to TC effects) within 0.2 degrees can be neglected when averaging over a large dataset. However, background variability can contaminatge the TC signal for larger horizontal constraints (e.g. 0.5 degrees). Furthermore, horizontal velocities within western boundary ocean currents (e.g. Gulf Stream) and geostrophic vortices within TC regions are typically on the order of O(10-100) cm/s (Shay et al., 1998). These currents can effectively transport a float more than 0.2 degrees away from its original position on the timescales of our TC analysis. Thus, the maximum 0.2 degree spatial constraint largely filters these floats from our results, so that we do not contaminate the TC analysis with transient effects of larger-scale dynamics.

3) All of the Argo pairs are within ±8 degrees relative to the center of the storm track, perpendicular to the storm's direction of translation. Thus 16 degrees is assumed to be the maximum cross-track scale of the area affected by TCs. This constraint is a first-order assumption, and we will analyze the horizontal scale of the globally-averaged TC response extensively in the results section.

We define TC-induced ocean thermal changes calculated from Argo pairs using the functional form：

$$dT_a = dT_a(ID, track, dist, depth, \delta t)$$

where *ID* identifies the particular storm, *dist* is the distance between the observation location and the track center perpendicular to the storm's direction of motion (the cross-track distance in the storm coordinate system), *track* denotes the spatial location of an Argo pair related to a TC-track (the along-track distance in the storm coordinate system), *depth* denotes the vertical depth of the temperature anomalies, and δt is the time difference between the observing time of the TC-affected Argo profile and the time of the nearest track center. We define the positive values of *dist* to be consistent with the asymmetric inertial response (to the right in the northern hemisphere and to the left in the southern hemisphere), referred to as *TC-Track* coordinates (Price et al. 2008).

To create a composite representation of the average ocean response, we reduce the 5-dimensional function dT_{a1} to a 3-demesional function by averaging the anomalies over all TC conditions corresponding to two predefined categories (TS/TD and Hurricanes). We define a track-averaged footprint of ocean thermal changes over all tracks, and we separate the events into two distinct categories: TS/TD and Hurricanes. Track locations with maximum wind speeds less than 63 knots are categorized as TS/TD, and all others are categorized as Hurricanes (this hurricane category represents conditions when a TC is in hurricane status). The footprint is represented as:

$$F_{TSTD}(dist, depth, \delta t) =$$

$$\sum_{i=1}^{i=n_{TSTD}} dT_a^i(ID, track, dist, depth, \delta t)] / n_{TSTD}(dist, depth, \delta t)$$

$$F_{Hur}(dist, depth, \delta t) =$$

$$\sum_{i=1}^{i=n_{Hur}} dT_a^i(ID, track, dist, depth, \delta t)] / n_{Hur}(dist, depth, \delta t)$$

In these equations, the dT_a is the observational temperature anomaly. The number of the temperature anomalies at each *dist*, *depth* and δt is denoted as n_{TSTD} and n_{Hur} for TS/TD and Hurricane respectively.

We construct the 3-dimensional footprints by grouping temperature anomalies from TS/TD and Hurricanes respectively with dimensions: *dist* containing 0.5 degree bins from -8 degree to +8 degree across the track, δt containing 0.5 day bins from 0 to 20 days, and *depth* containing 10m bins from 5m to 1000m and 50m bins from 1000m to 2000m. In each grid-box, averages of the temperature anomalies are calculated by using temperature anomalies from this box and 14 other adjacent bin-boxes (in *time* and *dist* dimensions between -0.5 to 0.5 day, and -1 to 1 degrees relative to the given box).

We use this strategy to capture the main variability of the ocean response and to avoid potential biasing caused by the un-even distribution of Argo pairs in space and time. Key points of this methodology include: 1) categorizing the events into weak and strong events/conditions, and 2) focusing on the cross-track temperature response, using a footprint technique that neglects along-track variability. Point 2) reflects the assumption about the importance of the asymmetric cross-track thermal response compared to along-track directions, which has been noted in numerous previous case studies (Black and Dickey, 2008; Deal, 2011; Price et al., 2008). However, recent studies (Jaimes and Shay, 2010; James et al., 2011) suggest ocean variability along the track can substantially modulate the ocean cooling response to TC forcing and distort the temperature anomaly in the wake of the storm, which can be important within western boundary currents and associated geostrophic vortices. As a first step to determine TC effects on upper ocean thermal structure on a global scale, we focus primarily on the cross-track ocean response.

As stated previously, our methodology requires the distance between two Argo profiles in a pair to be less than 0.2 degree. However, we do not require the pre-storm and post-storm measurements to be recorded from the same float. This criterion is in contrast to recent regional analysis using Argo data (Park et al., 2011), who stipulated the constraints that: two profiles are to be measured by the same Argo float in order to reduce the float-to-float calibration difference, and the maximum distance between measurements to be less than 200km. In the current study, ~80% of the pre-storm and post-storm measurements are from the same float.

Figure 1 shows the geographical distribution of the TC tracks along with all of the Argo pairs from January 2004 to December 2012, highlighting the global coverage of the Argo pairs in TC-affected regions (4410 total pairs). Tropical cyclones have

preferred locations and directions of motion. For example, TCs in the northwestern Pacific move to the northwest between 10-20^{o}N and northeast between 20-40^{o}N. This preferred storm location and direction of motion results in coastal pairs in the northwestern Pacific located on the left side of tracks, while the pairs away from the coast are typically located on the right side of the tracks. In the northeastern Pacific, TCs generally move to the northwest, leading to a clear distribution of right-side pairs in 20-40^{o}N and left-side pairs in 0-20^{o}N. Similarly, in the north Atlantic, the distribution of TCs leads to the left-side pairs mainly distributed between 0-15^{o}N and 40-50^{o}N. But in the Indian and Southern Pacific Ocean, the left and right side pairs mix together. These preferred locations of TCs and the resulting distributions of Argo pairs (Figure 2) can affect the geographical patterns of the TC-induced oceanic response.

The distributions of Argo pairs are presented in Figure 3 for the category, observation time (relative to storm passage), depth, and distance from storm center. Figure 3 reflects several key features of the methods and analysis, including: 1) the uneven distribution of the data; 2) the larger number of Argo pairs for the TS/TD conditions than Hurricanes (TS/TD conditions are much more common); 3) the number of Argo pairs decreases with time (e.g. we sample more pairs between 0-10 days after storm passage compared to 10-20); and 4) we obtain the least number of pairs near storm centers. Point 4) may be due, in part, to unreliable Argo measurements associated with severe conditions near storm centers (bad profiles) and/or strong horizontal currents (~100 cm/s) advecting the floats away from the storm centers. To check whether there are some systematic differences (i.e. drifting) of horizontal distance between the two profiles in a pair, we calculate the horizontal difference between the two profiles as in Appendix C. In both geographical coordinates and track coordinates, we find no significant effects of drifting.

The footprint method outlined above features several key methodological limitations, which include: (i) neglecting along-track TC-induced ocean variability; (ii) lack of Argo float comparisons within individual storms due to poor sampling at these spatial and temporal scales; and (iii) the effect of background ocean variability at specific sampled locations, which is difficult due to the sparseness of the floats and frequency of the measurements. A sensitivity test on the effect of background variability is presented in Appendix A, indicating that there is no significant systematic bias

induced by background variability when using the footprint method.

2.3 Estimation of ocean heat content changes during 0-3 days after storm passage

Since the air-sea exchanges in the TC affected regions within 0-3 days of the storm passage are dominated by TCs effects, which is several times larger than the background air-sea heat exchanges, it is reasonable to assume that the net ocean heat change within the TC-affected regions during this period is totally induced by TCs. Our choice of 3 days is to, at least partially, average out any float drift caused by inertial oscillations. This strategy is based on the notion that the ocean must be the energy source of a storm, so the total heat loss in the ocean during the storm is transported to the air as air-sea heat flux during the storm passage (0-3 days). The averaged OHC change is calculated as follows (in *Watts)*:

$$QA_{TSTD} = L_{track-TSTD}[\int_{dist=-8}^{dist=8} \frac{1}{T_{3days}} \int_{\delta t=0}^{\delta t=3} \int_{depth=0}^{depth=1200} \rho c_p F_{TSTD}(dist, depth, \delta t) d_{depth} d_{\delta t} d_{dist}] / T_{year}$$

$$QA_{Hur} = L_{track-Hur}[\int_{dist=-8}^{dist=8} \frac{1}{T_{3days}} \int_{\delta t=0}^{\delta t=3} \int_{depth=0}^{depth=1200} \rho c_p F_{Hur}(dist, depth, \delta t) d_{depth} d_{\delta t} d_{dist}] / T_{year}$$

where c_p is heat capacity of sea water ~4186 J/kg°C; ρ is density of sea water, which are calculated by using Argo salinity, pressure and temperature measurements before the storm; T_{year} is the duration of one calendar year in seconds, to calculate an annual mean; $L_{track\text{-}TSTD}$, $L_{track\text{-}Hur}$ - averaged track length within one year, about $1.4*10^8$ m, $8.3*10^7$ m for TS/TD and Hurricanes respectively, which are obtained by averaging the track length from 2004 to 2012.

We choose the time period between 0-3 days, because it likely captures the majority of the air-sea heat exchange during storm passage. However, other mechanisms may also influence air-sea heat flux in this time period, such as storm induced cooling via mixing and wave generation. TC-induced surface cooling can cause a reversal of surface fluxes in the days following storm passage, which marks the transition between the forcing stage and the recovery stage. Some studies suggest fluxes may reverse sign around 2 days after TC passage (Dare and McBride, 2011; Lloyd and Vecchi, 2011). The exact timing of this reversal depends on many factors, such as

storm intensity, translation speed and regional conditions, and the best choice is unclear in a global context. We performed sensitivity tests of the TC response to different choices of the time length (0-2, 0-2.5, 0-3.5 and 0-4 days), but the results (not shown), and the results and interpretations are generally consistent for all time scales.

2.4 Estimation of air-sea fluxes during TC passage

We examine the air-sea heat transfer rate in the TC-affected regions, by averaging air-sea heat flux as follows (in *Watts/m*^{2}):

$$H_{TSTD} = QA_{TSTD} /(L_{track-TSTD} \times R)$$

$$H_{Hur} = QA_{Hur} /(L_{track-Hur} \times R)$$

where R is the cross-track size of the TC-affected region which is set to be 16 degree (±8 degrees across the track). The other variables are consistent with QA_{TSTD} and QA_{Hur}.

2.5 Estimation of net ocean heat content changes

We estimate the net OHC changes by examining the average temperature response between 4 to 20 after storm passage, referenced to pre-storm conditions. We choose 20 days as the maximum duration, because sea surface temperatures are typically restored by this time, and it is difficult to separate TC effects from seasonal signals on timescales greater than 3 weeks. Sensitivity tests for the different choices of the time length are also conducted (4-18, 4-19 and 4-21 days). The results of these tests (not shown) suggest the magnitude of the TC signal is relatively insensitive to the choice of timescales for the time periods considered.

We calculate OHC changes using (in *Watts)*:

$$QN_{TSTD} = L_{track-TSTD}[\int_{dist=-8}^{dist=8} \frac{1}{T_{17days}} \int_{\delta t=4}^{\delta t=20} \int_{depth=0}^{depth=1200} \rho c_p F_{TSTD}(dist, depth, \delta t) d_{depth} d_{\delta t} d_{dist}]/T_{year}$$

$$QN_{Hur} = L_{track-Hur}[\int_{dist=-8}^{dist=8} \frac{1}{T_{17days}} \int_{\delta t=4}^{\delta t=20} \int_{depth=0}^{depth=1200} \rho c_p F_{Hur}(dist, depth, \delta t) d_{depth} d_{\delta t} d_{dist}]/T_{year}$$

where T_{17days} is the duration of 17 days in seconds. The other variables are the same to those in calculating QA_{TSTD} and QA_{Hur}.

Limitations of this methodology include:

1) The net OHC changes induced by TCs are averaged within 4-20 days after storm passage, which represents the restoration stage. However, the ocean changes may not be fully restored during this time interval. As noted previously, we choose this time period because TC signals are difficult to separate from the background seasonal cycle on longer time scales.

2) The internal waves generated by TCs induce fluctuations in temperature, which could potentially bias our results. However, we hypothesize that these wave effects average to zero because we are using a large number of Argo pairs (~4410).

3 Results and Discussion

Here we present the 3-Dimensional footprint maps for two time intervals, 0-3 days and 4-20 days referenced to storm passage. The 0-3 day interval represents about two inertial periods and reflects the direct ocean response to storm forcing (Sanford et al., 2011). We choose 3 days as an upper limit to the forced stage based on the following methodological constraints, limitations and uncertainties: 1) TC track information is every 6-12 hours, and Argo data may be offset by several hours due to its ascent speed; together these effects can lead to observational offsets up to 1 day; and 2) The inertial period changes rapidly with latitude in TC-affected regions (from 1 to 3 days). Considering these uncertainties, we choose 3 days as an approximation on the forced stage on the global scale, which represents the initial period of the TCs' influence on upper-ocean properties. We have conducted additional sensitivity tests to the choice of forced stage time interval using -1 to 2 days relative to storm passage, and the results are generally consistent to what we show here.

After 4 days, the ocean typically begins recovering to pre-storm and/or climatological conditions. While this restoration period can persist from weeks to months (Mei et al., 2013; Mei and Pasquero, 2013), this analysis averages the thermal response between 4 and 20 days after storm passage to estimate the mean ocean response during the recovery stage. Anomalies for both forced and recovery stages are referenced to pre-storm conditions as discussed in the methods section.

The amount of data for each footprint composite for the two time periods is shown in Figure 4. In the upper 100m, the number of measurements is generally more than 30 in each 0.5 degree box except near the storm center. The measurements generally decrease with depth especially deeper than 1000m, 1200m and 1500m (parking depths).

3.1 0-3 days footprint of ocean thermal changes

During storm passage, in the so-called forcing stage (Price et al., 1994), the cyclonic winds generally pump cold water up to the surface near the storm eye (Ekman pumping) and generate divergent currents in the upper ocean. To compensate the upwelling, down-welling away from the track occurs over a large area, appearing as ocean warming in the subsurface regions. The upwelling and down-welling oscillate

with a near-inertial period (Price, 1983), which has been termed "inertial pumping" (Shay et al., 1998). Meanwhile, the strong and sudden disturbance of storm winds generates near-inertial horizontal currents (Shay and Elsberry, 1987), which have both horizontal and vertical velocity shear, leading to cold-water entrainment at the base of the mixed layer.

The detailed vertical structure of ocean interior responses to hurricanes and TS/TDs are presented in Fig. 5a,c, where the significant signals are isolated compared with background variations. The standard errors are shown in Figure 5b,d. Figure 5 shows that both hurricanes and TS/TDs induce an asymmetric sea surface cooling with pronounced cooling on the right side of the track (in track coordinates). A much weaker pattern is found on the opposite side, supporting the asymmetry of the ocean response documented previously in the literature. These near surface cooling signals have uncertainties (standard errors in Figure 5b,d) with magnitudes of less than 40% of the signals. The rightward-biased cooling in the track coordinate system near the surface is also found in previous studies (left side in the southern hemisphere) (Dare and McBride, 2011; Price, 1981, 1983; Sanford et al., 2011; Dickey et al., 1998) due to the stronger vertical shear in right side of the track. This mechanism contributes ~80% of the SST response (Price et al., 1994). Another cooling mechanism besides of the shear instability is the turbulence generated also by wind stress (Chan and Kepert, 2010). Both are irreversible processes that produce mixed layer deepening. The mixing transports heat vertically from sea surface to the subsurface, appearing as a subsurface warming corresponding to the near-surface cooling, which is apparent in Figure 5 with a peak at ~50-100m.

Figure 5 shows a subsurface (30-200m) cooling within 1 degree of the track, and a subsurface warming on the both sides of the track between ±2 to 4 degrees from the storm center, consistent with previous results (e.g. Price, 1981; Sanford et al., 2011). These warming signals contain relatively large uncertainties (the standard error ranges from 40% to 100% of the absolute value of the signals) compared with surface signals, partly because they occur within the thermocline which exhibits higher variability. Our composite analysis of the response from Argo floats confirms that there is an Ekman pumping effect in the upper ocean (upper 200m), in that we observe a residual vertical motion within 1 degree of the storm track, appearing as a net column-averaged cooling near the storm center, along with down-welling outside the

storm center according (Figure 5a and b). It is also possible that instantaneous wind erosion plays a role in addition to upwelling (Jacob and Shay, 2003; James et al., 2011) for the upper ocean changes (upper 200m), in particular during slower storms that produce weaker near-inertial velocity responses. Despite smoothing out of inertial oscillations, the resultant subsurface warming is observable.

At depths greater than 200m, we find a weak cooling signal near the storm center and weak warming away from the storm. The weak cooling near the storm center (between -1 and +1 degrees) is significant down to 400m for hurricanes and 200m for TS/TD. These signals have large uncertainties, with standard errors up to 100% of the signals (Figure 5d). The causes for these deep ocean responses is beyond the scope of this study, but they may be linked to vertically propagating waves (Ascani et al., 2010; Sriver et al., 2013). Comparison of the TC thermal response with background oceanic variability indicates that the major structure of TC-induced thermal changes is significant compared with the background variability, as highlighted by black lines in Figure 5a,c.

The cross-track footprint of the oceanic thermal response is averaged over depth (0-1200 m) during days 0-3 days relative to storm passage (Figure 6), and we highlight the different characteristics of the response of the upper ocean (0-20 m) versus the entire column depth. Near the surface (0-20m), for hurricanes, the cooling spreads to a large area of ±5 degrees from the storm center with a peak around ~ -1.1^{o}C. In contrast, for TS/TD, we observe less cooling over a smaller area (a peak of ~ -0.5^{o}C). The sea surface anomalies estimated by Argo observations are consistent with other SST observations presented by multiple previous studies (Lloyd and Vecchi, 2010, 2011; Mei and Pasquero, 2013)

For the response of the entire ocean column, TS/TD generally cause cooling between -1° and +3° in storm coordinates, implying that the dominant mechanism affecting column-integrated temperature changes in TS/TD-affected regions is surface fluxes. The wind-driven entrainment itself does not change the ocean heat content of the whole water column, instead re-distributing the heat vertically via mixing. Ocean currents also advect mass and heat from its origin to different locations but do not change the net ocean heat content. Therefore, if there is a net ocean heat content change over TC-affected region, it must be via the ocean-atmosphere surface heat fluxes. A significant heat flux is also found in previous studies (Bell et al., 2012; Lin

et al., 2009b; Mcphaden, 2009), and we expand on this discussion in the next section.

For hurricanes, the water column experiences a cooling within ±2 degree of storm center, and stronger warming near between +2 and +4 degrees along the right side of the track (in track coordinates). Both cold and warm peaks are significant at the 90% confidence level according to the Null-hypotheses tests (Appendix B). This implies that there is a net heat transport from the storm center to the right side of the storm relative to the storm's direction of motion. The magnitude of column-averaged cooling (within +2 degree of the storm center) is greater than the warming along the right side (+2~4 degree), thus the net effect is a cooling of the upper ocean through enhanced surfaces fluxes.

3.2 Estimate of air-sea heat flux

Here we calculate a global estimate of air-sea heat exchange during TCs by integrating the ocean heat differences within storm-affected regions during a 3-day interval surrounding storm passage. We assume that during this period, the net column-integrated ocean heat loss is caused by heat transfer from the ocean to the atmosphere. We use the footprint methodology, which has two spatial dimensions: vertical depth and cross-track distance relative to the storm's direction of motion. Thus the footprint represents a 2-dimensional insulated box that is ±8 degrees across the storm track relative to the storm center and 1200m deep, with an opening at the air-sea interface. The heat exchange between the box and its surroundings occurs only at the surface.

To test whether assumptions about the footprint hold, particularly related to insulation from horizontal advection at the sides of the box and vertical heat exchange at the base, we calculate the box-averaged air-sea heat flux at different horizontal and vertical spatial scales, ranging from dx = ±1 degree to ±15 degrees (with 0.5 degree increment) and dz = 100m to 1900m (with 200m increment). As shown in Figure 7, the averaged air-sea heat flux stabilizes for dx > ~6 degrees. The decreasing trend for dx > ~7 degree is a 'dilution' effect, which is caused by enlarging the box size while the OHC change within TC-affected region remains unchanged. Note this effect is generally linear for large dx, which is expected since the depth is held constant. In the vertical direction, the air-sea flux estimates are unchanged for dz greater than 700m

(corresponding to dx > ~5 degrees). This result suggests the method requires at least ±7 degree and 700m in order for the insulated box assumption to be considered valid. Thus, we use a terminal depth *dz*=1200m based on the availability of data in the upper ocean (a large portion of Argos stop near 1200m), and *dx*=8 degrees.

The annual contribution of TCs to the air-sea heat fluxes for *dx*=8 degrees and *dz*=1200m is about ~4.80 W/m^2 and ~6.25 W/m^2 for TS/TD and Hurricanes, respectively. The positive heat flux represents the net ocean heat loss. We calculate the total global air-sea heat exchange in Figure 8. Given the methodology described previously, the integrated heat transport should converge to the total TC contribution as we increase the domain size. Consistent with Figure 7, this convergence occurs for dx > ~6 degrees. For TS/TD, heat exchange continues to increase to dx > 9. However, this increase is probably not caused by TCs given the large spatial scale. Therefore, we estimate the global annual air-sea heat exchange during TCs to be 1.05 PW and 0.82 PW for TS/TD and hurricanes, respectively. The total heat transfer is 1.87 PW annually, which represents the total heat loss from ocean to atmosphere during the forced stage (0-3 days).

The global air-sea fluxes derived in Figure 7 correspond to 584 W/m^2 for TS/TD and 761 W/m^2 for hurricanes, when averaging fluxes within storm-affected regions (± 8 degrees across the track). These values are consistent with previously published case study estimates, such as the mooring observations during the category-4 hurricane Nargis (Lin et al., 2009; Mcphaden et al., 2009), which estimated storm-induced air-sea fluxes of ~400-900 W/m^2. Furthermore, our global estimates are consistent to first order with the estimated heat required to bring the troposphere into thermodynamic equilibrium (Emanuel, 1991) with the ocean ~10^8 J/m^2, which is equivalent to ~3 W/m^2 annually over the global ocean basin. This estimate generally agrees with our results (4.80W/m^2 and 6.25W/m^2 for weak and strong storm categories respectively). A recent observational study (Bell et al., 2012) shows that the mean TC enthalpy fluxes from CBLAST field program increases from 764 W/m^2 at wind speeds of 52 m/s (category 3) to 2189 W/m^2 at wind speeds of 72 m/s (category 5) near the storm center. The result of the category 3 conditions is similar to our estimate averaging over all hurricanes (category 1 to 5). In addition, Braun, (2006) estimates a 1.34 PW heat loss from the ocean caused by hurricanes, which is ~0.52 PW larger than our estimates. Trenberth and Fasullo, (2007) estimates the TC-induced

enthalpy exchange caused by hurricanes is about 0.58 PW in total for 1990-2005, ranging from 628 W/m^2, 703 W/m^2, 783 W/m^2 and 895 W/m^2 to 1019 W/m^2 for categories 1 to 5 respectively, where the category-3 estimate is similar to our estimates averaged over all hurricane conditions. In total, their result is about 0.24 PW smaller than our result for similar conditions. As noted previously, the three day averaging period used here may capture some of the recovery stage associated with a reversal of air-sea fluxes and the reheating of anomalously cold surface waters after storm passage, thus these results may be considered slightly conservative compared to previous estimates (e.g. Braun, 2006).

The geographical patterns of the TC-induced air-sea heat fluxes are presented in Figure 9, using spatial and temporal averaging consistent with our global estimates. We find significant spatial variability in the flux estimates, with the largest fluxes occurring in regions with the most TC activity (e.g. northwestern Pacific). These results indicate the zonally averaged TC contribution to the total annual air-sea enthalpy flux budget may be as large as ~9.1 W/m^2, with peak value of 20 W/m^2 at latitudes experiencing the most TCs. These fluxes could account for as much as ~10% of the total annual ocean latent heat flux (90-110 W/m^2) (Trenberth et al., 2009) derived using NCAR/NCEP reanalysis (Kalnay et al., 1996), shown as the black curve in Figure 9b.

As a simple check of the TC contributions of net surface fluxes, we compare the results from Argo data to the background surface fluxes using the NCEP/NCAR reanalysis. Specifically, we calculate the net climatological air-sea heat fluxes along TC tracks using NCEP/NCAR reanalysis for the same Argo sampling criteria (dx=8 degrees, dt=0-3 days). However, these climatological fluxes represent the daily averages over a 20-year period (1990-2012), rather than from specific TC days. In other words, the plot shows the surface fluxes along storm tracks for non-TC conditions. The NCEP/NCAR reanalysis product generally predicts a net oceanic heat uptake in background climatological conditions during TC seasons (Figure 9c). In the absence of TCs, typical conditions would favor a net ocean heat uptake, on the order of 1 W/m^2 zonally averaged across the global ocean. This background warming signal is of opposite sign to the TC effect, which tends to cool the ocean through enhanced surface fluxes during the forcing stage.

Figure 9a shows a prominent peak in air-sea heat flux in the Western Pacific Ocean,

reaching values as large as 65 W/m^2. Because this region experiences the most TC activity, this peak is probably due to more TCs occurrences relative to other regions. In Figure 10a and b, we present the frequency at each 1^o by 1^o grid box which is affected by TCs per year, given the affected regions (cross-track distance) defined to be ±1 and ±8 degrees relative to storm center. As expected, the figure shows a higher frequency of TC occurrences in grid boxes as we increase the size of the affected region. For example, in the western and eastern Pacific Ocean, between 1 and 1.5 storms pass directly through a single 1^o by 1^o grid box annually, but this activity can contribute to as much as 12~14 storms affecting the same grid boxes when we increase the TC-affected region to ±8 degrees.

To check whether the peak in heat flux is caused by increased frequency of TCs, we assume that one grid box can be affected by only one storm within 20 days. The annual air-sea heat fluxes for this method are presented in Figure 11, showing the peak fluxes in the northwestern Pacific decrease to 30 W/m^2 while the overall fluxes in the other basins are relatively unaffected (to within ~5-10 W/m^2). Since the nature of air-sea heat exchanges is complicated by the close proximity of storms in active TC regions, such as in northwestern and northeastern Pacific, our geographical map of air-sea heat flux should be regarded as a first-order approximation.

Here we use a bootstrap technique to constrain the error bars and characterize the uncertainties of our heat flux and OHC estimates. Beginning with the total number of Argo float samples (4410 pairs), we randomly choose 90% of pairs and repeat our air-sea heat flux and anomalous OHC calculations, as described in the previous sections. We repeat the calculation 200 times. In Fig.12b, d, 200 estimates of air-sea heat fluxes presented as function of horizontal footprint size of the TC-affected regions (distance to the storm center). Most of these bootstrap estimates exhibit similar patterns with those shown in Figure 7, supporting the robustness of our estimates. We choose an error bar of one standard deviation near 8 degree to quantify the uncertainty of our estimate. This uncertainty measure is equal to ±0.85 W/m^2 for TS/TD and ±1.50 W/m^2 for Hurricanes, which is equivalent to ~20% and ~25% of the fluxes for TS/TD and hurricanes, respectively. Or, in terms of global annual heat flux, this uncertainty equates to ±0.20 PW for TS/TD and ±0.21 PW for Hurricanes (Fig.12a, c), which is equivalent to ~20% and ~25% of the total estimates for TS/TD and Hurricanes, respectively. Including these uncertainties, our estimates of air-sea

heat flux during the TC forcing stage (0-3 days relative to storm passage) are: 1.05±0.20 PW (4.8±0.85 W/m^2) for TS/TD and 0.82±0.21 PW (6.25±1.5 W/m^2) for hurricanes.

3.3 4-20 days footprint of ocean thermal changes

After storm passage, radiative forcing and ocean currents tend to restore the storm-induced surface anomalies. Past studies show that upper-ocean thermal anomalies can persist on the order of: 10-20 days (Price et al., 2008), 20-30 days (Dare and McBride, 2011), or even longer than 30 days (Mei et al., 2013; Mei and Pasquero, 2013; Park et al., 2011). Differences in timescales likely depend on differences in regional and seasonal ocean conditions (i.e. when and where TCs occur). Surface cooling is typically restored within 20 days according to satellite observations (Hart et al., 2007a), while thermal effects within the ocean interior may persist on inter-seasonal timescales (Jansen et al., 2010; Park et al., 2011). The mechanical energy is dispersed by continuous mixing near the surface and within the thermocline, as well as propagating internal waves to the larger ocean basin (Shay et al., 1989), with a delay of about 5-10 days (Price et al., 1983).

The vertical structure of the general temperature response between 4 and 20 days after storm passage, relative to pre-storm conditions, is shown in Figure 13. Weak cooling still dominates the subsurface (100m-200m) response near the storm center. But the standard error can be 100%-150% of the signal, maybe because of the longer time window (17 days in total). This weaker subsurface cold anomaly compared with the 0-3 days response implies that cooling caused by upwelling is going to be restored on timescales of 20 days, and this signal may be associated with the geostrophic ridge that develops in the wake of storm following the dispersion of near-inertial waves (Geisler, 1970). In addition, the near-surface cold anomaly along the right-side of the storm is still apparent during this restoration stage, thus pointing to the persistence of the TC signal.

Figure 13 shows persistent warm anomalies between 20 and 200m along both the right and left sides of the storm tracks, which are greater in magnitude than the observed forced stage response (0-3 days), with typical standard error (as a percentage of the TC signal) of 30%-70% for TS/TDs and 30%-90% for Hurricanes. However,

we do not find similar temperature anomaly structures in the background variability for high TC activity basins (e.g. west Pacific), even when extending the background pairs selection criteria to 40days and 60days. It may also be possible that TCs directly affect the boundary current structure, such that there is warm advection into the TC-affected regions after storm passage as the boundary current returns to its climatological (or pre-storm) state. In this case, our methodology prohibits analyzing direct effects of TCs on the background state, since TCs and background variability are examined separately from different sets of Argo pairs. Thus, any potential dynamical connections between TC forcing and the large-scale currents are beyond the scope of this study.

Figure 14 shows the vertical profile of the spatially averaged (-6 to +6 degrees) thermal response during the TC recovery stage relative to pre-storm conditions. We find vertical mixing and upwelling/downwelling induces significant cooling near the surface (0-20m depth) and subsurface warming within the upper thermocline (50-200m) for both TS/TD and hurricanes. The signals deeper than 200m exhibit relatively weak cooling, and they are only significant for Hurricanes near the storm center. As noted by previous studies, deep ocean (below 400m) thermal responses are rarely observed. One observation down to 530m (Price, 1981) shows a large oscillation with amplitude about 30m at the depth of 530m after 10 days of storm passage. A study using a mooring observation (Brink, 1989) observed a TC-induced temperature oscillation at depths around 1000m. Because of the lack of observations, further modeling and theoretical studies are needed to understand the response of the interior ocean to extreme surface wind forcing below 200m.

3.4 Estimates of net OHC changes after storm

Net OHC changes are estimated by calculating the difference between the average post-storm temperature during wake recovery (between 4 and 20 days after storm passage) and the pre-storm conditions. We choose 20 days as the upper limit of the post-storm temperature, because it reflects the average time scale of SST recovery after storm passage. Temperature anomalies are plotted in Figure 15 as a function of the spatial and vertical extents of the TC footprint. Within 3 degrees of the storm center, both TS/TD and Hurricanes induce column-averaged cooling at all depths. The

cooling effect decreases for increasing footprint size, approaching zero for TS/TD and a net warming for Hurricanes. This result suggests that upwelling and heat loss to the atmosphere near the storm center are partly (for TS/TD) or fully (for Hurricane) compensated by post-storm surface fluxes. Furthermore, when the footprint size is larger than 8-9 degrees, the absolute value of the average temperature anomalies decreases, which is again attributable to the 'dilution' effect as discussed in the previous section. The temperature anomalies also converge for increasing depth, when the footprint is greater than 3 degrees. Thus, we use a cross-track length scale of ~8 degrees and depth scale of 1200 meters to quantify the TC-induced upper ocean thermal response. The average temperature anomalies for these footprint length scales are $+0.039^{o}$C for Hurricanes and -0.0125^{o}C for TS/TD.

The annual contribution of the net TC-induced changes in global OHC is calculated by multiplying the net ocean temperature changes with yearly averaged track lengths. This method is based on our results that the averaged ocean thermal change over all storms between post-storm (after recovery) and pre-storm conditions is 0.039^{o}C and -0.0125^{o}C for Hurricanes and TS/TD, respectively. The positive values indicate heat gained by the ocean. These estimates correspond to global annual flux contribution of ~ 5.98 W/m^2 (0.75 PW) for Hurricanes and ~ -1.90 W/m^2 (-0.41 PW) for TS/TDs, where the positive values represent oceanic heat convergence and negative flux represents the net oceanic heat loss. This implies that after hurricanes, the ocean keeps on warming, and recovers the storm-induced enthalpy flux during the storm passage.

These findings indicate the total TC contribution to the global ocean heat convergence is estimated to be 0.34 PW annually in 2004-2012 periods, which reflects a net ocean heat gain from the atmosphere due to all storms.

Our results suggest that weak storms (TS/TD) tend to cool the ocean, while hurricanes tend to warm the ocean, when considering both storm-induced and post-storm fluxes. The difference in the ocean response may be due to the relatively weak vertical ocean mixing and surface cooling induced by TS/TD compared to hurricanes. For TS/TD, the OHC change is likely driven by the storm-induced enthalpy fluxes during passage. Because weaker storms typically cause less vertical mixing and thus less significant cold wakes following storms, there will be less post-storm heat flux into the ocean during the wake recovery stage. Conversely, strong events (hurricanes) induce more vertical mixing and surface cooling, which leads to more heat flux into the ocean

during the recovery stage and thus net oceanic heat convergence. This finding supports previous results using altimetry (Mei et al., 2013) and simplified approaches based on sea-surface temperature changes (Sriver and Huber, 2007 and Jansen et al., 2010).

It is important to note that this estimate averages the post-storm temperature between 4 and 20 days after storm passage. As a test of this assumption, we can also define the post-storm restoration period to be when the OHC change is to zero. In other words, post-storm warming balances the storm-induced enthalpy flux. Our estimates suggest that the OHC restoring period for hurricanes is less than 20 days but more than 20 days for TS/TD.

Similar to calculating the uncertainties of 0-3 days OHC change, the 200 estimates of TC-induced OHC changes are shown in Figure 16. We choose the uncertainty to be equivalent to the standard deviation of the average temperature change for spatial extent of 8 degree and 1200 m, consistent with the heat flux estimate. This uncertainty equates to $\pm 0.0063^{o}C$ for TS/TD and $\pm 0.0143^{o}C$ for hurricanes, which represents ~50% and 36% of the estimated OHC changes for TS/TD and hurricanes, respectively. Considering this uncertainty, our estimates of TC-induced thermal changes are: $-0.0125 \pm 0.0063^{o}C$ for TS/TD and $0.0390 \pm 0.0143^{o}C$ for hurricanes. Equivalently, these estimates correspond to global annual heat flux of -0.41±0.21 PW (-1.90±0.96 W/m^2) for all TS/TDs, and 0.75±0.25 PW (5.98±2.1 W/m^2) for all hurricanes, where the positive values denote a net oceanic heat convergence.

4 Caveats

The methodology presented here contains several key caveats and limitations. One outstanding question relates to the accuracy of the no-TC pairs in capturing the inter-annual variability in the timing of events. In other words, given that years with tropical cyclones are likely to have different positioning/intensity of major atmospheric circulation patterns such as subtropical highs, one could expect to see a Rossby wave response from such shifts resulting in potentially anomalous trends at depth. To address this issue, we conducted the following test:

TC-affected pairs are subdivided into two subsets: one contains data from 2004-2008 and the other from 2009-2012. We subdivide storms to analyze sensitivity of our footprint results to different spatial patterns of storm locations. The results for TS/TD and Hurricane 4-20 days footprints are presented in Figure 17, both compared with the 2004-2012 results in black contours. In the figure, the main pattern is similar for the two time periods, with only some strength differences of the signals. In addition to this test, we calculate footprints of the background pairs for the two periods (not shown), and the differences are within the limit of insignificant noise. Results support the notion that the background signals can be mostly smoothed out by using footprint strategy when averaging over large amounts of data with variant time and spatial distributions.

An additional caveat relates to vertically propagating waves forced by the storms. For example, mooring data has shown evidence of vertically propagating Rossby waves. Unfortunately, our method may not be able to distinguish the effects of these evanescent waves due to the following: (i). These non-permanent signals may be filtered by averaging a large amount of data over a long period of time, and (ii). We do not observe any such wave structure or patterns in our analysis (such as thermal anomaly across track in Figure 5, 13). However, the potential effect of vertical propagating waves on upper-ocean temperature and energy budgets remains an active area of research (Ascani et al., 2010; Sriver et al., 2013).

Ocean stratification varies regionally, which can in turn pose problems for estimating global averages of ocean responses to TCs. To quantify the effect of regional variability, we calculate TC-induced ocean thermal changes within 4-20 days within three ocean basins separately: Pacific Ocean, Indian Ocean and Atlantic Ocean. Note,

we also subdivide the Pacific basin into separate regions – Western/Eastern/Southern Pacific). Figure 18 shows the results in the footprint composite format. Key findings include: (i) The global-averaged thermal footprint pattern (Figure 13c) is generally consistent with the pattern in Pacific Ocean, especially in Western Pacific (Figure 18a,d), since there are ~2500 pairs from the Pacific Ocean (or roughly ~60% of the total number of pairs globally); and (ii) Although the footprint within the Atlantic and Indian Oceans have large uncertainties, key characteristics of the general patterns are robust, such as ocean cooling near the storm center from surface to subsurface (0-200m) and subsurface warming along both sides of the track (Figure 18e,f). However, only 25% and 15% of the Argo pairs globally are sampled from the Indian Ocean and Atlantic Ocean respectively, thus physical interpretations are limited by the relative lack of data. (iii) In the Eastern Pacific, the ocean responses seems to be different from other regions, which appears cooling at the left side of TC as shown in Figure 18b. This difference may be due to the lack of data in this region, indicating that our method is insufficient to reconstruct the local responses to TCs.

5 Conclusions

We use Argo data to create a global representation of TC-induced changes in upper ocean temperature, using a new footprint method to create a composite analysis of the vertical profile of the cross-track ocean temperature response for two distinct time scales (0-3 days and 4-20 days relative to storm passage) and categories (TS/TD and hurricanes), and we include all TCs occurring globally from 2004-2012. We find this method is capable of capturing the main characteristics of TC-induced ocean variability related to cross-track and intensity variations, as well as the differences in the response due to the choice of time scales (e.g. forcing versus recovery).

We find that during the storm passage, the ocean generally experiences a net heat loss to the atmosphere through storm-induced enthalpy fluxes. Our observational results suggest that TCs contribute 11.5 W/m^2 (1.87 PW) heat in TC-affected regions annually from the ocean to the atmosphere within 0-3 days after storm passage. Of this total, weak storm (TS/TD) contribute 4.80 W/m^2 (1.05 PW) and strong storms (hurricanes) account for the rest. The uncertainty of our estimate is about 20% for TS/TD and 25% for hurricanes.

Recent in-situ, remotely sensed and reanalyzed air-sea heat flux products (Smith et al. 2011) have faced challenges in closing the ocean heat budget. These analyses show a net global oceanic heat gain of 20-30 W/m^2 (Josey et al., 1999), while the global mean net heat flux is ~0.5 W/m^2 from observed variations in OHC. Our observational results suggest that TCs may provide a potential mechanism (heat flux in high wind regime) for filling this gap.

After storm passage, ocean conditions in TC-affected regions experience a recovery process to at least partially restore upper ocean conditions pre-storm or climatological values through enhanced air-sea fluxes leading to ocean heat convergence. This recovery stage lasts much longer than the forcing stage during the storm passage. We estimate the net changes in a time scale of 4-20 days relative to pre-storm conditions, which implicitly includes fluxes during the forced stage. On this time scale, around ~ 0.75 PW (5.98 W/m^2) of heat is transferred annually from atmosphere to the ocean for hurricanes, which represents a net ocean heat gain after storms. However, TS/TD exhibit an opposite response, ~ -0.41 PW (1.90 W/m^2), representing a net ocean heat loss for weaker events. We estimate the uncertainty to be about 50% of our estimates

for TS/TD and 35% for Hurricanes. The opposite sign of net OHC changes after storm (4-20 days) for weak and strong storms implies the impact of these events on the upper ocean is sensitive to the intensity. This result also suggests that additional atmospheric heating due to anthropogenic warming may potentially increase the rate of TC-induced ocean heat uptake, since research suggests the number of strong TCs may increase with continued warming (Bender et al., 2010; Knutson et al., 2010).

To assess the TC contribution to historical trends in the ocean heat uptake, we calculate the total air-sea heat flux in each year from 1970 to 2010, by assuming that each TS/TD transfers 6.25 W/m^2 and each hurricane transfers 4.8 W/m^2 heat from the TC-affected region to the atmosphere during 0-3 days after storm. The annual heat flux is shown in Figure 19 in blue. The figure shows a maximum atmospheric heating ~12×10^{22} J during 1996~1997 and a generally larger signal between 1988 and 1998, which is due to more TC activity during these years. As suggested in Trenberth and Fasullo, (2007), the large El Nino activity during these years (3 between 1990-1995 and a large event in 1997-1998) may be at least partially responsible this boost in activity in key TC regions (e.g. west Pacific).

Figure 19 also shows the accumulated TC-induced net OHC changes in recovery stages (4-20 days) relative to pre-storm conditions, which shows the net affect of storms on OHC. We assume the net OHC effect is -1.9 W/m^2 for TS/TD and 5.98 W/m^2 for hurricanes (positive value shows a net heat gain by the ocean). Net OHC changes show that TC-induced ocean heat convergence is increasing since 1970. This OHC change is likely due to the increase in the fraction of strong storms during the past 40 years (Knutson et al., 2010). The linear trend of TC-induced ocean heat uptake is about 0.046×10^{22} J/year, which is 11% of global ocean heat uptake of the upper-most 2000 meters during the past 55 years (~0.42×10^{22} J/year) (Levitus et al., 2012).

In summary, the ocean response to TCs is complex. It is not a simple surface cooling and subsurface warming everywhere in TC-affected regions. It is highly variable, with upwelling/divergent currents near the storm center and down-welling/convergent currents in the outer regions, entrainment in the mixed layer, inertial oscillation of vertical/horizontal currents (Price, 1983), and maybe other differences in the response due to TC characteristics such as translation speed (Emanuel, 2007). Our results indicate that TCs are an important component in the ocean system, providing a link

between variability in air-sea heat flux and ocean heat uptake.

Appendix A: Estimation of background variability in Argo pairs

Isolating the TC-induced thermal changes using Argo floats is difficult, because biases can arise due to changes in the thermal structure of the background ocean state. These biases can be caused by many processes such as: the seasonal cycle, meso-scale signals and large-scale spatial variability. Here we employ a test to examine potential biases and quantify background errors related to our footprint method described in the previous sections. Background noise is estimated by using Argo pairs under quiescent conditions (i.e., without TCs), hereafter denoted as NoTC-pairs.

Our methodology for analyzing background variability is outlined in the following steps:

1) We collect all Argo profiles during Jan. 2004- Dec. 2012 for which there are no TCs within ±8 degree distance of their location and -50 to +5 days relative to storm passage. These profiles are denoted as NoTC-profiles.

2) Background Argo pairs are formed by using these NoTC-profiles. The sampling strategy is the same as the TC pairs. One Argo pair consists of two Argo profiles, which are within 0.2 degree and 20 days. 20 days is set here to make this time scale comparable with the time scale of the typical TC response. We tested the sensitivity of the analysis to the choice of time scale, by also analyzing variability out to 40 days. The results were consistent for both time scales.

3) The pairs are then spatially and temporally chosen according to TC track and TC-affected pairs. In each 4^o by 8^o grid box and 1 month time period during each year, if there is at least one TC-affected pair, background pairs detected in step 2) are flagged as 'legal-NoTCpair' and all of the un-flagged pairs are removed. By using this strategy, all of the remaining pairs (NoTC-pairs) are comparable to the TC-affected pairs for all locations and dates. Thus for each storm track, background pairs are collected across all years corresponding to storm track locations and timing of events (within a given year). This sampling strategy provides a consistent method for analyzing background variability, by comparing Argo pairs from the same regions and times of year during storm (TC-pairs) and non-storm (NoTC-pairs) conditions.

4) To frame the background signals into the context of our footprint method, the NoTC-pairs obtained in step 3) are converted to a background footprint (denoted as *NoTC-TSTD-footprint* and *NoTC-Hur-footprint* for TS/TD and Hurricane

respectively). To summarize the method, each TC-footprint bin, for example F_{TSTD} with a bin denoted by (*dist, depth, δt*), contains *n* TC-affected pairs with geographical locations of (lat_i,lon_i) *i*=1:*n*. The *NoTC-TSTD-footprint* (*NoTC-Hur-footprint)* at the same bin (*dist, depth*, *δt*) is calculated by selecting *m* NoTC-pairs according to the locations of TC-affected pairs. If there exists a NoTC-pair within 2 degrees to (lat_i,lon_i), this NoTC-pair is selected to calculate the *NoTC-TSTD-footprint(dist, depth*, *δt)* (*NoTC-Hur-footprint(dist, depth*, *δt)*). In the construction of the background footprint, *m* is set to *n*. In this case, we define background variability at a single location in terms of one NoTC-pair. Using one NoTC pairs corresponding to a given TC pair enables strict comparison between the two data sets. Otherwise, the method will yield more weight to individual pairs from locations with low TC activity (e.g. where there are many NoTC pairs compared to TC pairs). However, we have performed additional tests using all of the pairs from step 3), and the results are generally consistent with the constraints employed here.

By using the background pairs selected as above, both the *NoTC-TSTD-footprint* and *NoTC-Hur-footprint* are obtained according to the footprint method proposed in the previous section. In this case, the background signals can be directly comparable to the TC footprint (F_{TSTD} and F_{Hur}).

In total, 13701 pairs are collected after step 3) is conducted. All the Argo profiles are under the same quality control procedures as the TC-affected Argo profiles discussed in the previous section. Figures A1a, b display the total amount of TC-pairs and NoTC-pairs in each 4^o by 8^o degree grid boxes. The spatial distribution of NoTC-pairs is generally consistent with the TC-affected pairs.

The errors and biases due to the presence of background variability are quantified using two independent methods described in the following subsections. We first conduct a gross check on background error, and we quantify the background error using the footprint method.

Gross Check. By applying a gross check, we are aiming to check the magnitude of the global-averaged background signals and the size of the background uncertainties in TC-affected regions and seasons. We also compare the error with standard Argo accuracy of ~0.005^oC. We define the temperature differences of these NoTC-pairs as background noise (dBT_a) using the functional form:

$dBT_a = dBT_a\ (time, \delta t, depth, lat, lon)$

where *time* denotes the Julian day of the reference Argo profile; δt is the time difference between the two Argo profiles in each pair; *lat* and *lon* denote the spatial locations of a pair; and *depth* is the depth of a temperature anomaly. These anomalies are collected in two maps to test for any systematical temporal or spatial biases in background pairs:

Back-Map1 (*depth*)=

$$\int_{day1}^{day_2}\int_{\delta t_1}^{\delta t_n}\int_{lat1}^{lat2}\int_{lon1}^{lon2} dT_{a1}(day, \delta t, depth, lat, lon)\, d_{lon} d_{lat} d_{\delta t} d_{day} / n(depth)$$

Back-Map2 (δt)=

$$\int_{day1}^{day_2}\int_{depth_1}^{depth_n}\int_{lat1}^{lat2}\int_{lon1}^{lon2} dT_{a1}(day, \delta t, depth, lat, lon)\, d_{lon} d_{lat} d_{depth} d_{day} / n(\delta t)$$

where $n(depth)$ and $n(\delta t)$ denote the number of pairs for each depth and each δt respectively. In *Back-Map1*, all of the background temperature anomalies are grouped into bins representing 5 meters thickness between 0m to 2000m depth. In *Back-Map2*, temperature anomalies are grouped into temporal bins of size 0.5 days between 0 and 20 days.

The mean and ±1 standard deviation of the background noise as a function of *depth* and δt are presented in Figure A2. The means of the background noise with depth are near zero with a very small positive temperature anomaly near the sea surface (20-100m with the peak about 0.005^{o}C), which may be caused by seasonal/meso-scale signals. However, this anomaly is negligible compared to TC signals (discussed in the following sections).

The means of the background variability as a function of time also show no trend with δt (Figure A2b) for 0-1000m (also no trend for 0-20m, not shown here). The 0-1000m averaged standard deviations of Argo pairs influenced by Hurricanes and TS/TD show a 0.1-0.2^{o}C larger deviation compared to estimates of background variability, which shows that TCs can disturb normal ocean conditions and that the perturbation is observable using this methodological framework.

Next, we apply a bootstrap analysis to determine the effect of sample size on characterizing potential biases, errors, and background variability. At each depth, we

randomly choose a certain number of pairs (the number of samples changes from 10 to 9000, with a step size of 20), and we calculate the mean of the temperature anomalies of the chosen pairs. This procedure is repeated 200 times yielding 200 means, and we calculate the standard deviation of the 200 means at each vertical level. Figure A3a shows the standard error at different depths against sample sizes, indicating the error of the temperature anomalies decrease with sample size. When sample sizes are greater than 400, the standard error at depths deeper than 400m is less than 0.02^{o}C. and at depths less than 400m the standard error is less than 0.06^{o}C. Both of these errors are less than 5% of standard deviations at corresponding depths shown in Figure A3a. When the sample size is increased, the error is gradually reduced and converges near the Argo sensor accuracy (0.005^{o}C) for the upper shallow depths and below the Argo sensor accuracy for deeper levels. This result suggests that increasing the amount data generally reduces the background error when averaged over large areas.

We consider the time evolution of background noise by randomly choosing a specific number of pairs (the number changes from 10 to 900, with a bin size of 20) and calculate the mean of the selected samples. This procedure is also repeated 200 times, and then we calculate the standard deviation of the 200 time means. Figure A3b shows the standard error for different times as a function of sample sizes, showing a consistent error at different times in general. For sample sizes greater than 200, the standard error is generally less than 5% of the standard deviations shown in Figure A3b (e.g. less than 0.03^{o}C for all time differences). Considering that the Argo accuracy is ~0.005^{o}C, the error we detected is several times larger than the Argo accuracy.

Background footprint. To be consistent with our method for quantifying TC-induced ocean thermal changes, we construct a similar footprint that is a composite based on background pairs. *NoTC-TSTD-footprint* and *NoTC-Hur-footprint* is presented for two time periods: 0-3 days and 4-20 days for TS/TD and Hurricane respectively (Figure A4). For TS/TD locations, the background thermal anomalies for the two time periods show no clear pattern at any depths or spatial locations across the track. Since these background pairs are selected according to the dates and locations of TC-affected pairs but in different years, we conclude that the footprint method produces no significant background patterns.

The standard deviations of the *NoTC-TSTD-footprint* and *NoTC-Hur-footprint* is presented in Figure A5, corresponding to the mean of background footprints shown in Figure A4. It appears that the standard deviations (SD) show a similar vertical distribution for the two time periods and storm categories. In the upper 20m, typical SD values are around 0.4^{o}C. From 20-200m, we find larger SD values between ~0.6 and 1.2^{o}C, and SD decreases below 200m. The background SDs for TS/TD locations show larger values below the surface (20-200m) than for hurricane locations. However, none of these figures show a systematical distribution of SDs across the storm track, thus suggesting again no substantial background biases. We detect a slight bias along the left side of the storm tracks within background SD for both TS/TD and Hurricane locations, which may be due in part to the presence of more coastal pairs on the left side of TC tracks in high activity TC regions.

These tests of the background variability show that background errors are generally small at all depths considered here (between 0 and 2000 m) and time scales (between 0~20 days) compared to the TC signals (discussed in the following sections), and we find no significant background biases using the footprint strategy. We will use these results as the basis (i.e. null hypothesis) for testing the significance of the observed TC effects in the following section.

Appendix B: Null-hypothesis test on Argo data

Here we present a null-hypothesis test to analyze whether the proposed footprint method is capable of capturing the tropical cyclone signals compared to the background variability. Our hypothesis is that the detected TC signals are significant compared to background noise. The null-hypothesis is that the TC-induced signal is the average of background noise (H_0: $\mu=B$, where B is the mean of background noise). The alternative hypothesis claims TC-induced signals are either higher or lower than the average of the background noise (H_1: $\mu\neq B$).

A two-sided *z*-test is conducted to test the hypothesis. Sampling distributions of the means (SDM) are used to assist in analyzing the results. Assuming the null-hypothesis is true, the sampling distribution of TC-induced signals (denoted as 'x') based on sample counts (denoted as 'n') will be normally distributed with a mean of background mean (B) and standard error of ($\sigma/\sqrt{n}$), where σ is the standard deviation

of background noise. Therefore, under hypothesis H_0, the observed 'x' should be: x-N(u, $\sigma/\sqrt{n}$). We want to find an interval (x^-, x^+) for x, which would lead to the acceptance of the null hypothesis. To meet this need, we calculate: $x^+ = z_{stat}*SEM+B$ and $x^- = -z_{stat}*SEM+B$, where z_{stat} quantifies how far x is from B in standard deviation units. Here the value of z_{stat} corresponds to a probability threshold (or p-value) of 0.05. The value of 0.05 means the observed signals is 'highly significant' within 95% confidence interval, if they are outside the interval of (x^-, x^+). SEM is the standard error ($\sigma/\sqrt{n}$).

Based on this strategy, we calculate the 'highly significant' intervals for temperature anomalies as a function of depth and distance respectively (shades in Fig. 6, 14), and for the footprint (thick solid contours in Figure 5, 13). In brief, the confidence interval in Figure 5 and 13 is calculated by $x^+ = z_{stat}*SEM+B$ and $x^- = -z_{stat}*SEM+B$ at each grid box. σ is the standard deviation of background noise calculated in Figure A5, and the background mean (B) is shown in Figure A4. Sample counts n is the number of TC-pairs at each grid box.

To obtain confidence intervals for Figure 6 and 14, the mean (B) and standard deviation (σ) of background noise with time and depth are calculated as in Figure A2. While those for distance are set manually based on the notion that the background noise is confirmed to be white noise. The background mean with distance is set to zero, and the standard deviation is set to the mean of standard deviations at the first 3 days.

Appendix C: Test on the horizontal distances of the two Argo floats in a pair

In this study, 0.2 degree is selected as the maximum horizontal distance between the reference-Argo and TC-affected Argo, since evidence suggests this choice will minimize the influences of the strong background signals (such as meso-scale eddys, strong Kuroshio, Califonia Currents, and internal waves). Ideally our footprint strategy aims to detect the ocean thermal changes at a fixed position. But to obtain a satisfied amount of pairs, the 0.2 degree criteria is used, thus there is the potential for sampling biases associated with horizontal and vertical motions on upper ocean currents. Therefore, it is necessary to test whether the selection of pairs within 0.2 degree influences our main results.

Here we compare the position of floats before and after storms from each TC-affected pair by using two coordinate systems. This test is conducted for Same-float pairs (i.e. the two profiles in a pair are both measured by the same float) and Different-float pairs separately (i.e. the two profiles in a pair are measured by two different floats). One test uses latitude-longitude (Fig.A6a), and the other test uses track coordinates (Fig.A6b), and both coordinate systems use the location of the float before the storm as the origin. The post-storm float position appears to be randomly distributed around the initial pre-storm position. We examine the drifting direction along and across the track at different distances from the float to the track center, where the distance between pre-storm and post-storm Argo is calculated in track coordinates. Fig.A7 shows that floats drift moderately but systematically in the water under forces of TCs, and a float tends to move away from the storm track (Pink), and move backward along the storm track (Red). However, we cannot explain these movements using the current methods, due to dynamical effects such as: surface wind forcing, near-inertial currents, and mean currents at Argo parking depths. But we find no systematical drift distance for Different-float-pairs. Since the maximum systematical drift within 20 days is less than 5km, this distance is relatively small compared to the maximum displacement distance of 20km. Therefore, we assume horizontal motions of the floats do not affect our essential results. Approximately, 17% of pairs used in our analysis are considered Different-float-pairs.

Furthermore, it is worth noting Argo profiles affected by TCs may potentially be labeled as poor quality data in the Delayed Mode Quality Control process (Yu et al., 2010), since data is typically rejected if there are dramatic changes in temperature or salinity profiles. In this study we include the real-time Argo profiles as well as the delayed-mode data. However, we do not attempt to recover wrongly labeled data.

Acknowledgments. This work is supported by the project “Structures, Variability and Climatic Impacts of Ocean Circulation and Warm Pool in the Tropical Pacific Ocean” of National Basic Research Program of China (Grant No.2012CB417404) and Chinese Academy Sciences’ Project “Western Pacific Ocean System: Structure, Dynamics and Consequences” (Grant No. XDA10010405).

References

Ascani, F., Firing E., Dutrieux P., McCreary J. P., and Ishida A.: Deep Equatorial Ocean Circulation Induced by a Forced-Dissipated Yanai Beam. J Phys Oceanogr, **40,** 1118-1142, 2010.

Bell, M. M., Montgomery M. T., and Emanuel K. A.: Air-sea enthalpy and momentum exchange at major hurricane wind speeds observed during CBLAST. J Atmos Sci. doi:10.1175/jas-d-11-0276.1, 2012.

Bender, M. A., Knutson T. R., Tuleya R. E., Sirutis J. J., Vecchi G. A., Garner S. T., and Held I. M.: Modeled impact of anthropogenic warming on the frequency of intense Atlantic hurricanes, Science, **327**, 454-458. doi: 10.1126/science.1180568, 2010.

Black, W. J., and Dickey T. D.: Observations and analyses of upper ocean responses to tropical storms and hurricanes in the vicinity of Bermuda. J Geophys Res-Oceans, **113**. doi: 10.1029/2007JC004358, 2008.

Braun, S. A.: High-resolution simulation of Hurricane Bonnie, 1998. Part II: Water budget, J Atmos Sci, **63**, 43-64, 2006.

Brink, K. H.: Observations of the Response of Thermocline Currents to a Hurricane. J Phys Oceanogr, **19,** 1017-1022, 1989.

Camargo, S. J., and Sobel A. H.: Western North Pacific tropical cyclone intensity and ENSO. J Climate, **18,** 2996-3006, 2005.

Chan, J. C., and Kepert J. D.: Global Perspectives on Tropical Cyclones: From Science to Mitigation. World Scientific Publishing Company, **4,** 94, 2010.

Cione, J. J., and Uhlhorn E. W.: Sea surface temperature variability in hurricanes: Implications with respect to intensity change. Mon Weather Rev, **131,** 1783-1796, 2003.

D'Asaro, E. A.: The ocean boundary layer below Hurricane Dennis, J Phys Oceanogr, **33**, 561-579, 2003.

1 Dare, R. A., and McBride J. L.: Sea Surface Temperature Response to Tropical
2 Cyclones. Mon Weather Rev, **139,** 3798-3808, 2011.

3 Deal, R.: Surface Heating and Restratification of the Ocean After a Tropical
4 Cyclone. Electronic Theses, Treatises and Dissertations**,** Paper 60, 2011.

5 Dickey, T., and Coauthors: Upper-ocean temperature response to Hurricane Felix as
6 measured by the Bermuda testbed mooring. Mon Weather Rev, **126,** 1195-1201,
7 1998.

8 Emanuel, K.: Environmental factors affecting tropical cyclone power dissipation, J
9 Climate, **20**, 5497-5509. doi: 10.1175/2007jcli1571.1, 2007.

10 Emanuel, K. A.: The theory of hurricanes, Annu Rev Fluid Mech, 23, 179-196, 1991.

11 Emanuel, K. A.: Thermodynamic control of hurricane intensity, Nature, **401**, 665-669,
12 1999.

13 Emanuel, K.: Contribution of tropical cyclones to meridional heat transport by the
14 oceans. J Geophys Res-Atmos, **106,** 14771-14781, 2001.

15 Fedorov, A. V., Brierley C. M., and Emanuel K.: Tropical cyclones and permanent
16 El Nino in the early Pliocene epoch. Nature, **463,** 1066-U1084, 2010.

17 Freeland, H., Roemmich, D., Garzoli, S., LeTraon, P., Ravichandran, M., Riser, S.,
18 Thierry, V., Wijffels, S., Belbéoch, M., Gould, J., Grant, F., Ignazewski, M.,
19 King, B., Klein, B., Mork, K., Owens, B., Pouliquen, S., Sterl, A., Suga, T.,
20 Suk, M., Sutton, P., Troisi, A., Vélez-Belchi , P. and Xu, J.: "Argo - A Decade
21 of Progress" in Proceedings of OceanObs'09: Sustained Ocean Observations
22 and Information for Society Venice, Italy, 21-25 September 2009, Hall, J.,
23 Harrison, D.E. & Stammer, D., Eds., ESA Publication WPP-306, 2009.

24 Geisler, J. E.: Linear theory of the response of a two layer ocean to a moving
25 hurricane. Geophys. Fluid Dyn., **1,** 249-272, 1970.

26 Ginis, I.: Tropical cyclone-ocean interactions. Atmosphere-Ocean Interactions, W.
27 Perrie, Ed., Advances in Fluid Mechanics Series, **33,** 83-114, 2002.

Hart, R. E.: An inverse relationship between aggregate northern hemisphere tropical cyclone activity and subsequent winter climate. Geophys Res Lett, **38**, 2011.

Hart, R. E., Bosart L. F., and Hosler C.: The possible seasonal climate impact from anomalous frequency of recurving tropical cyclones. Preprints, 19th Conf. on Climate Variability and Change, San Antonio, TX, Amer. Meteor. Soc., 6.3, 2007a.

Hart, R. E., Maue R. N., and Watson M. C.: Estimating local memory of tropical cyclones through MPI anomaly evolution. Mon Weather Rev, **135,** 3990-4005, 2007b.

Huang, P., Sanford T. B., and Imberger J.: Heat and turbulent kinetic energy budgets for surface layer cooling induced by the passage of Hurricane Frances (2004), J. Geophys. Res., **114**, C12023, doi:10.1029/2009JC005603, 2009.

Jacob, S. D., and Shay L. K.: The role of oceanic mesoscale features on the tropical cyclone-induced mixed layer response: A case study. J Phys Oceanogr, **33,** 649-676, 2003.

Jaimes, B., and Shay L. K.: Near-Inertial Wave Wake of Hurricanes Katrina and Rita over Mesoscale Oceanic Eddies. J Phys Oceanogr, **40,** 1320-1337, 2010.

James, B., Shay L. K., and Halliwell G. R.: The Response of Quasigeostrophic Oceanic Vortices to Tropical Cyclone Forcing. J Phys Oceanogr, **41,** 1965-1985, 2011.

Jansen, M. F., Ferrari R., and Mooring T. A.: Seasonal versus permanent thermocline warming by tropical cyclones. Geophys Res Lett, **37,** -, 2010.

Josey, S. A., Kent E. C., and Taylor P. K.: New insights into the ocean heat budget closure problem from analysis of the SOC air-sea flux climatology, J Climate, **12**, 2856-2880, 1999.

Lin, I. I., Pun I. F., and Wu C. C.: Upper-Ocean Thermal Structure and the Western North Pacific Category 5 Typhoons. Part II: Dependence on Translation Speed. Mon Weather Rev, **137,** 3744-3757, 2009a.

Lin, I. I., Chen C. H., Pun I. F., Liu W. T., and Wu C. C.: Warm ocean anomaly, air sea fluxes, and the rapid intensification of tropical cyclone Nargis (2008). Geophys Res Lett, **36**, 2009b.

Liu, Z., Xu J., Zhu B., Sun C., and Zhang L.: The upper ocean response to tropical cyclones in the northwestern Pacific analyzed with Argo data. Chin. J. Oceanogr. Limnol., **123–131**, 2007.

Lloyd, I. D., and Vecchi G. A.: Submonthly Indian Ocean Cooling Events and Their Interaction with Large-Scale Conditions. J Climate, **23,** 700-716, 2010.

Lloyd, I. D., and Vecchi G. A.: Observational Evidence for Oceanic Controls on Hurricane Intensity. J Climate, **24,** 1138-1153, 2011.

Mcphaden, J. M., Foltz, G. R., Lee, T., Murty V. S. N., Ravichandran, M., Vecchi G. A., Vialard, J., Wiggert J. D., Yu, L.: Ocean-atmosphere interactions during cyclone Nargis. EOS Transactions, American Geophysical Union, **90,** 53, 2009.

Mei, W., and Pasquero C.: Spatial and Temporal Characterization of Sea Surface Temperature Response to Tropical Cyclones. J Climate, **26,** 3745-3765, 2013.

Mei, W., Primeau F., McWilliams J. C., and Pasquero C.: Sea surface height evidence for long-term warming effects of tropical cyclones on the ocean. P Natl Acad Sci USA, **110,** 15207-15210, 2013.

Park, J. J., Kwon Y. O., and Price J. F.: Argo array observation of ocean heat content changes induced by tropical cyclones in the north Pacific. J Geophys Res, **116**, 2011.

Powell, M. D., Vickery P. J., and Reinhold T. A.: Reduced drag coefficient for high wind speeds in tropical cyclones, Nature, **422**, 279-283, 2003.

Price, J. F.: Upper Ocean Response to a Hurricane. J Phys Oceanogr, **11,** 153-175, 1981.

Price, J. F.: Internal Wave Wake of a Moving Storm .1. Scales, Energy Budget and Observations. J Phys Oceanogr, **13,** 949-965, 1983.

Price, J. F., Sanford T. B., and Forristall G. Z.: Forced stage response to a moving hurricane. J Phys Oceanogr, **24,** 233-260, 1994.

Price, J. F., Morzel J., and Niiler P. P.: Warming of SST in the cool wake of a moving hurricane. J Geophys Res-Oceans, **113,** -, 2008.

Sanford, T. B., Price J. F., and Girton J. B.: Upper-Ocean Response to Hurricane Frances (2004) Observed by Profiling EM-APEX Floats. J Phys Oceanogr, **41,** 1041-1056, 2011.

Smith, S. R., Hughes P. J., and Bourassa M. A.: A comparison of nine monthly air-sea flux products, Int J Climatol, **31**, 1002-1027. doi: 10.1002/joc.2225, 2011.

Shay, L. K., and Elsberry R. L.: Near-Inertial Ocean Current Response to Hurricane Frederic. J Phys Oceanogr, **17,** 1249-1269, 1987.

Shay, L. K., Elsberry R. L., and Black P. G.: Vertical Structure of the Ocean Current Response to a Hurricane. J Phys Oceanogr, **19,** 649-669, 1989.

Shay, L. K., Mariano A. J., Jacob S. D., and Ryan E. H.: Mean and near-inertial ocean current response to Hurricane Gilbert. J Phys Oceanogr, **28,** 858-889, 1998.

Sriver, R. L., and Huber M.: Observational evidence for an ocean heat pump induced by tropical cyclones. Nature, **447,** 577-580, 2007.

Sriver, R. L., and Huber, M.: Modeled sensitivity of upper thermocline properties to tropical cyclone winds and possible feedbacks on the Hadley circulation, Geophys Res Lett, **37**, L08704, doi:10.1029/2010GL042836, 2010.

Sriver, R. L., Huber M., and Chafik L.: Excitation of equatorial Kelvin and Yanai waves by tropical cyclones in an ocean general circulation model. Earth Syst Dynam, **4,** 1-10, 2013.

Sriver, R. L., Goes M., Mann M. E., and Keller K.: Climate response to tropical cyclone-induced ocean mixing in an Earth system model of intermediate complexity. J Geophys Res-Oceans, **115,** -, 2010.

Trenberth, K. E., Davis C. A., and Fasullo J.: Water and energy budgets of hurricanes: Case studies of Ivan and Katrina, J Geophys Res-Atmos, **112**(D23) , 2007.

Trenberth, K. E., Fasullo J. T., and Kiehl J.: Earth's global energy budget, B Am Meteorol Soc, **90**, 311-+, 2009.

von Schuckmann, K., and Le Traon P. Y.: How well can we derive Global Ocean Indicators from Argo data?, Ocean Sci, **7**, 783-791, 2011.

Willis, J. K., Lyman J. M., Johnson G. C., and Gilson J.: In Situ Data Biases and Recent Ocean Heat Content Variability. J Atmos Ocean Tech, **26,** 846-852, 2009.

Wright, C. W., Walsh E. J., Vandemark D., Krabill W. B., Garcia A. W., Houston S. H., Powell M. D., Black P. G., and Marks F. D.: Hurricane directional wave spectrum spatial variation in the open ocean, J Phys Oceanogr, **31**, 2472-2488, 2001.

Yu, T., Han G. J., Guan C. L., and Deng Z. G.: Several Important Issues in Salinity Quality Control of Argo Float. Mar Geod, **33,** 424-436, 2010.

Figures:

Figure 1. Tracks of tropical cyclones from Jan. 2004 to Dec. 2012, associated with the distribution of Argo pairs used in the paper. The colors of the tracks indicate the categories of tropical cyclone –tropical depression (TD; yellow), tropical storm (TS; orange), category 1-5 cyclones (denoted by red, magenta, purple blue, and black from category 1 to 5 respectively). The locations of Argo pairs are dotted in two colors: cyan dots are the pairs located at the right side of the corresponding TC-track, and green dots are the pairs located on the left side of the track. We analyze 885 tracks, and a total of 4410 Argo pairs.

Figure 2. Locations of TC-affected Argo pairs with colors showing the cross-track distances of their locations relative to the corresponding storm track. Positive values indicate pairs to the right (left) side of the track in Northern hemisphere (Southern hemisphere).

Figure 3. Histograms of the Argo float pairs for different statistics: a) storm category, b) time after storm passage (0.5 day bin), c) distance from the storm center (0.5 degree bin), and d) depth (10m bin). In c), positive distance represents the right (left) side of the track in Northern Hemisphere (Southern Hemisphere), and negative distance represents the left (right) side in Southern Hemisphere (Northern Hemisphere).

Figure 4. Count of TC-affected pairs in each 0.5 degree distance bin from -8^{o} to 8^{o} across the storm track for two footprint composites: TS/TD in the upper panel, Hurricane in the bottom panel. The statistics are conducted in two time periods: 0-3 days on the left, 4-20 days on the right.

Figure 5. 0-3 days averaged thermal changes (relative to pre-storm conditions) as a function of depth and distance, in TC track coordinates. a) TS/TD, between ±5 degrees from track center, the dashed contours interval is 0.1^{o}C, and the solid black contours isolate the 90% confidence interval of the signals. The standard error of the footprint is presented in b). c) is 0-3 days footprint for Hurricane, between ±7 degrees from track center, the dashed contours interval is 0.2^{o}C, and the solid black contours isolate the 90% confidence interval of the signals. The standard error of the footprint is presented in d). The unit is ^{o}C.

Figure 6. 0-3 days averaged temperature change as function of distance across the cyclone center for hurricanes (red) and TS/TD (blue), in TC track coordinates. The

values are smoothed using a 3 point (1.5 degrees) moving filter. Light blue shading shows the 90% confidence interval of background noise based on Null-hypothesis analyses for TS/TD, and the light pink shading is for hurricane. Surface temperature anomalies are presented as the thin curves, and thick curves show 0-1200m averaged temperature changes. The error bars are one standard deviation, which is calculated as follows: 90% percent of pairs are randomly selected, and then we calculate the thermal anomalies of these pairs. This process is repeated 200 times, so 200 samples of thermal anomalies are obtained, and the standard deviation is calculated from thermal anomalies of these 200 samples.

Figure 7. Estimates of air-sea heat flux within TC with different footprint domain sizes (horizontal and depth) for: a) TS/TDs and b) Hurricanes. The results of 1200m are highlighted in cyan.

Figure 8. The impacts of domain size on global annual heat transfer from the ocean to the atmosphere by TCs for: a) TS/TDs and b) Hurricanes. The colors are the same to those in Figure 7.

Figure 9. Geographical pattern of air-sea heat flux caused by TCs. a) Globally integrated net heat flux caused by TCs calculated using Argo float data (W/m^2). b) Zonally averaged TC-induced heat flux (red curve), compared with the annual climatology (1990-2010) of air-sea latent heat flux (black curve) derived from NCEP/NCAR reanalysis (Kalnay et al. 1996). c) Net surface flux (positive upward) along storm tracks for climatological conditions during the period 1990-2010 (W/m^2), derived from NCEP/NCAR reanalysis using storm tracks from 1990-2010. The plot represents the background air-sea flux contribution to the Argo analysis using the 20-year daily climatology. d) Zonal average of the climatological net surface heat fluxes shown in c.

Figure 10. Frequencies of tropical cyclones per year affecting 1^o by 1^o grid boxes, when the TC-affected region is assumed to be a) ±1 degree from the track center, and b) ±8 degrees from the track center.

Figure 11. Geographical distribution of air-sea heat flux caused by TCs. We assume each grid box can only be affected by 1 storm within a 20 day window.

Figure 12. 200 estimates on heat transport (in a) and c)) and air-sea heat flux (in b) and d)) based on 200 randomly selected samples of pairs. a) and b) are estimates under TS/TD conditions and b) and c) for hurricanes. The mean of 200 estimates is

highlighted in blue for TS/TD and in red for hurricane. Error bars represent the standard error.

Figure 13. Vertical profile of the 4-20 days averaged ocean thermal changes (referenced to pre-storm conditions) from the track center for: a) TS/TD between +5 and - 5 degrees and c) Hurricanes between +7 and - 7 degrees. The dashed contours interval in black is 0.1^{o}C for TS/TD and 0.2^{o}C for Hurricane. The solid black contours denote the signals that are significant at 90% confidence interval. b) and d) shows the standard error of the estimations corresponding to a) and c) respectively. The unit is ^{o}C.

Figure 14. Vertical temperature change averaged within the -6 to +6 degree range from storm center during the recovery stage (4-20 days) relative to pre-storm conditions. Blue and red lines represent TS/TD and Hurricanes, respectively. Also plotted are the 90% confidence intervals in Null-hypothesis test (light blue and light pink shading for TS/TD and hurricane, respectively). The light blue and pink curves show the mean background noise in TS/TD and Hurricane subsets respectively. The error bars represent the standard deviations, which are calculated by using the method as presented in Figure 6.

Figure 15. Column averaged temperature anomalies within 4-20 days after tropical cyclones, relative to pre-storm conditions, as a function of the horizontal box size across the storm track (from ±1 degree to ±15 degree) for: a) TS/TD, and b) hurricanes. The colors are different vertical size of the TC-affected box from 100m to 1900m. The results for the box with 1200m depth is highlighted in cyan.

Figure 16. 200 estimates (in cyan) of 0-1200m column averaged temperature as a function of distance across the storm track, based on randomly sampling 90% of the Argo pairs for: a) TS/TD and b) Hurricanes respectively. The mean and standard deviations are highlighted as the red line and error bars.

Figure 17. The 4-20 days averaged ocean thermal changes detected by using data from two year periods: 2004-2008 in the left panel and 2009-2012 in the right panel, shown in colors. The black contours are the result when using all of the data from 2004 to 2012, the same to the contours in Figure 13. The results of Hurricane are presented in the top panel and the bottom panel for TS/TD. The unit is ^{o}C.

Figure 18. Ocean thermal changes induced by hurricanes within 4-20 days after storm passage for individual ocean basins: a. in Western Pacific Ocean, b. in Eastern Pacific Ocean, c. in Southern Pacific Ocean, d. in Pacific Ocean, e. in Indian Ocean, f. in Atlantic Ocean. The black contour is the global-averaged hurricane-induced ocean thermal changes in 4-20 days, which is the same to that in Figure 13c. The unit is ^{o}C.

Figure 19. a): The annual TC-induced ocean heat loss via air-sea heat flux in 0-3 days (blue line) and the net ocean heat content changes after storm (in 4-20 days) (red line). The positive values show the net heat gain. The linear trend of the net ocean heat gain is presented in pink, and the trend is 0.046×10^{22} J/year. b): Yearly averaged track lengths for both TS/TD (blue) and hurricanes (in red).

Figure A1. Counts of the a) NoTC-pairs and c) TC-affected pairs in each 4^{o} by 8^{o} degree grid box.

Figure A2. Background ocean temperature variability as a function of depth and time. a) Mean (green curve) and one standard deviation (green shading) of background variability as a function of depth, compared with one standard deviation of hurricane and TS/TD affected pairs. b) Time evolution of background variability of 0-1000m average (light green line and light green shading for mean and standard deviation respectively). The standard deviations of temperature anomalies in Argo pairs under TS/TD and hurricane conditions are plotted in light blue and light red, respectively.

Figure A3. Bootstrap analyses of background noise. a) Standard errors at different depth versus sample numbers with colors denoting different depths. b) Standard errors at different times versus sample numbers with colors denoting different time. Solid lines are the results by using the whole NoTC-pairs dataset, and the dots show the same results for the TC-affected pairs.

Figure A4. Background ocean thermal changes as a function of depth and distance in TC track coordinates. The background footprint is created corresponding to TS/TD footprint a) on 0-3 days average and b) on 4-20 days average, and to Hurricane footprint c) on 0-3 days average and d) on 4-20 days average. The contours interval is 0.2^{o}C in black. The units are ^{o}C.

Figure A5. Standard deviation of the background footprints for TS/TD and Hurricane locations respectively on two time periods: 0-3 days and 4-20 days. The unit is ^{o}C.

Figure A6. Schematic scatter plots showing Argo floats drifting destination from the

origin. Two coordinate systems are: a) latitude-longitude, with the location of the float before storm as origin; b) Track direction as y-axis, and the location of the float before the storm as the origin. The red dots are the destination of the pairs with pairs from the same float in red (with the mean in red star) pairs from different floats in blue (with the mean in big blue dot).

Figure A7. Horizontal distance difference between the two profiles in a TC-affected pair along and across the track as a function of the distance from the float location to the track center. Here the distance is calculated in track coordinates, i.e: positive distance across the track represents the inertial-resonant side (right side in Northern hemisphere and left side in Southern hemisphere). The horizontal distances by using pairs that the two profiles are from different floats are shown in dark blue (along track) and light blue (across track), while drifting distances based on the remaining pairs are shown in purple (across track) and red (along track).

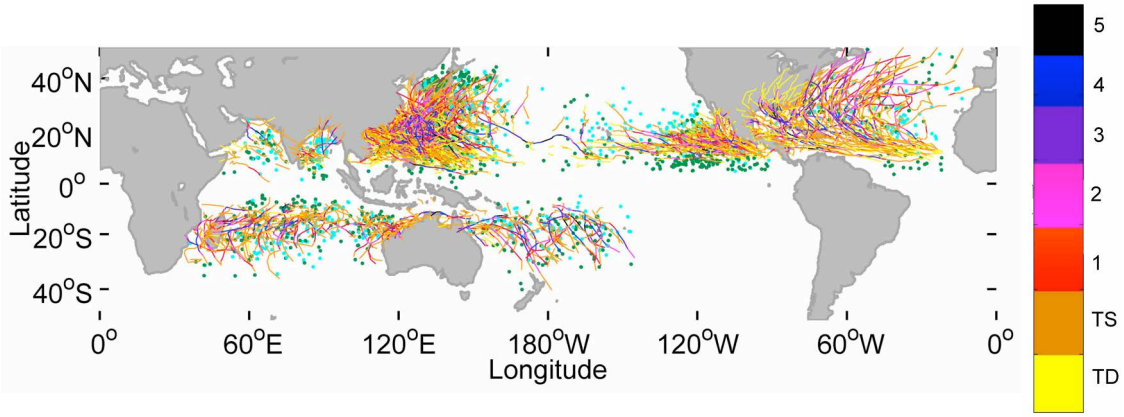

Figure 1. Tracks of tropical cyclones from Jan. 2004 to Dec. 2012, associated with the distribution of Argo pairs used in the paper. The colors of the tracks indicate the categories of tropical cyclone –tropical depression (TD; yellow), tropical storm (TS; orange), category 1-5 cyclones (denoted by red, magenta, purple blue, and black from category 1 to 5 respectively). The locations of Argo pairs are dotted in two colors: cyan dots are the pairs located at the right side of the corresponding TC-track, and green dots are the pairs located on the left side of the track. We analyze 885 tracks, and a total of 4410 Argo pairs.

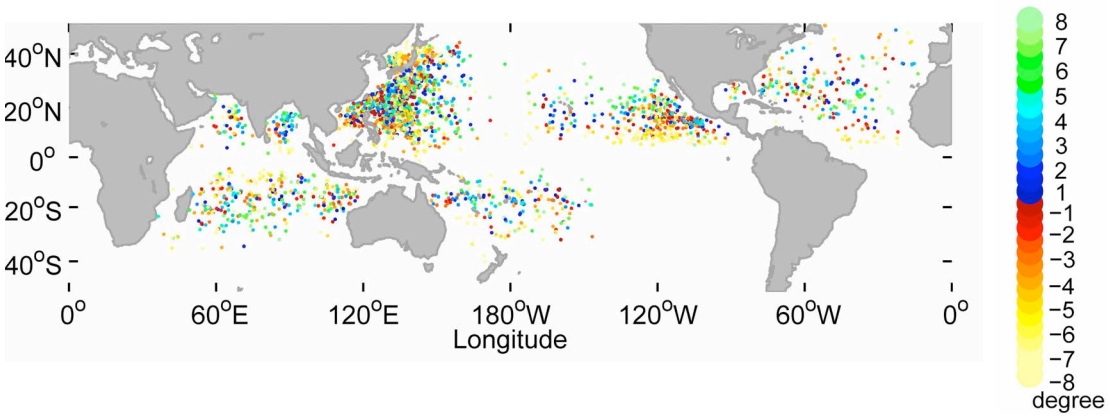

Figure 2. Locations of TC-affected Argo pairs with colors showing the cross-track distances of their locations relative to the corresponding storm track. Positive values indicate pairs to the right (left) side of the track in Northern hemisphere (Southern hemisphere).

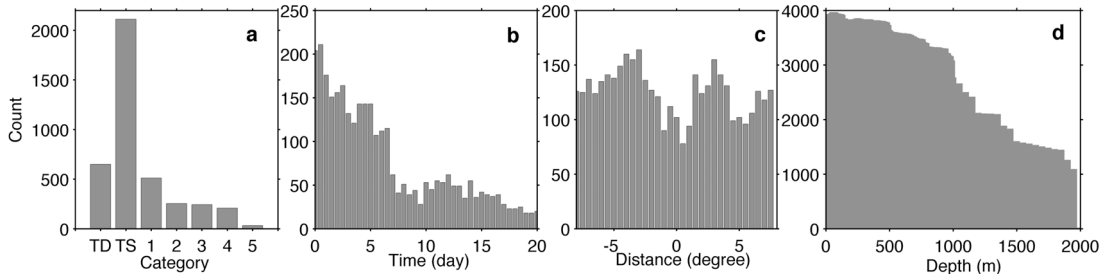

Figure 3. Histograms of the Argo float pairs for different statistics: a) storm category, b) time after storm passage (0.5 day bin), c) distance from the storm center (0.5 degree bin), and d) depth (10m bin). In c), positive distance represents the right (left) side of the track in Northern Hemisphere (Southern Hemisphere), and negative distance represents the left (right) side in Southern Hemisphere (Northern Hemisphere).

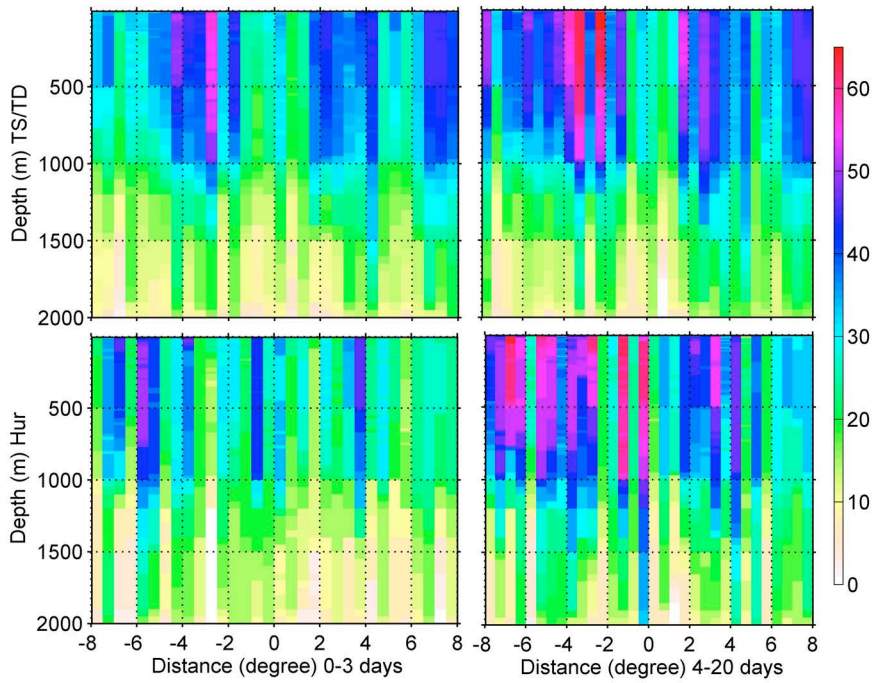

Figure 4. Count of TC-affected pairs in each 0.5 degree distance bin from -8^{o} to 8^{o} across the storm track for two footprint composites: TS/TD in the upper panel, Hurricane in the bottom panel. The statistics are conducted in two time periods: 0-3 days on the left, 4-20 days on the right.

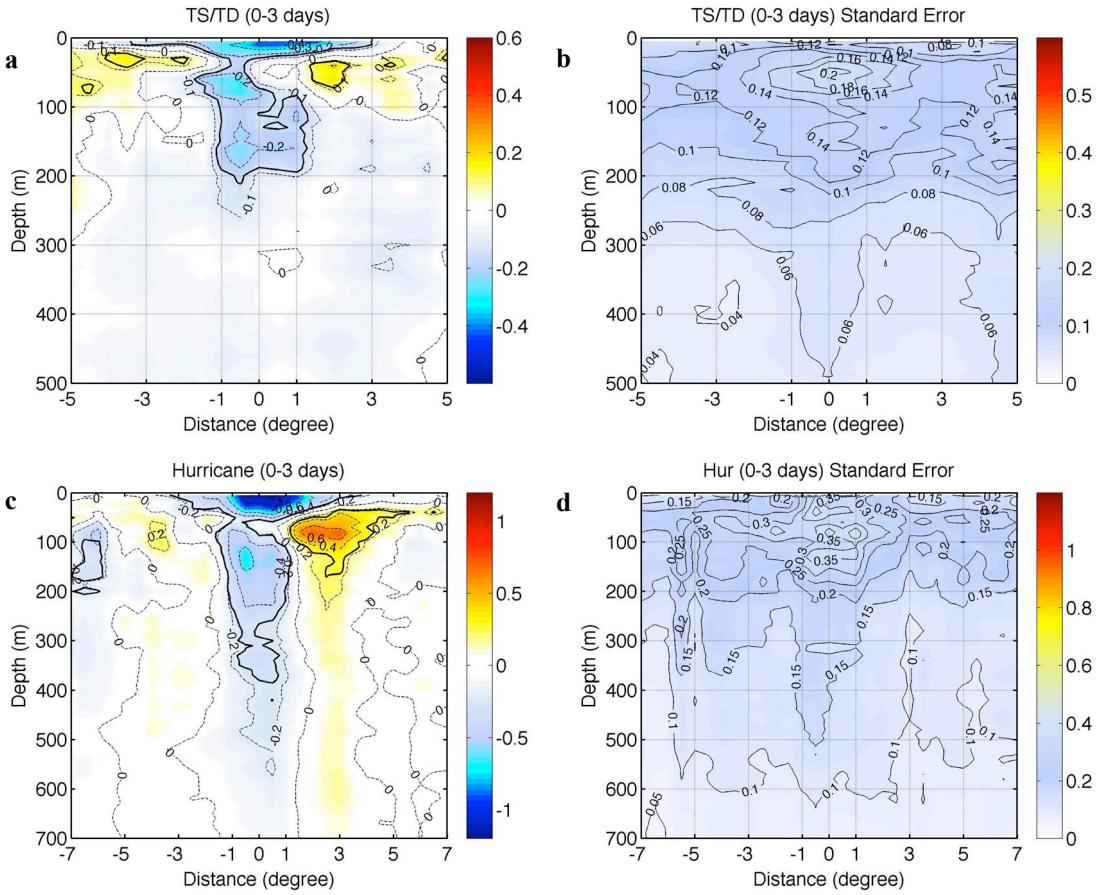

Figure 5. 0-3 days averaged thermal changes (relative to pre-storm conditions) as a function of depth and distance, in TC track coordinates. a) TS/TD, between ±5 degrees from track center, the dashed contours interval is 0.1°C, and the solid black contours isolate the 90% confidence interval of the signals. The standard error of the footprint is presented in b). c) is 0-3 days footprint for Hurricane, between ±7 degrees from track center, the dashed contours interval is 0.2°C, and the solid black contours isolate the 90% confidence interval of the signals. The standard error of the footprint is presented in d). The unit is °C.

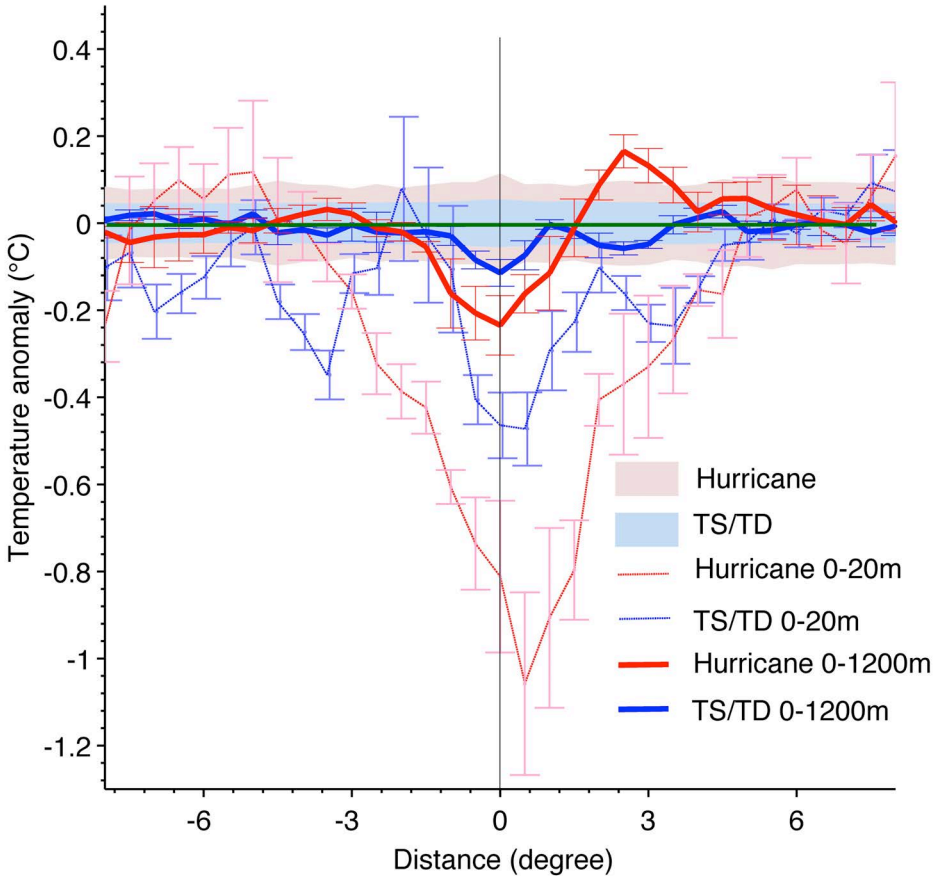

Figure 6. 0-3 days averaged temperature change as function of distance across the cyclone center for hurricanes (red) and TS/TD (blue), in TC track coordinates. The values are smoothed using a 3 point (1.5 degrees) moving filter. Light blue shading shows the 90% confidence interval of background noise based on Null-hypothesis analyses for TS/TD, and the light pink shading is for hurricane. Surface temperature anomalies are presented as the thin curves, and thick curves show 0-1200m averaged temperature changes. The error bars are one standard deviation, which is calculated as follows: 90% percent of pairs are randomly selected, and then we calculate the thermal anomalies of these pairs. This process is repeated 200 times, so 200 samples of thermal anomalies are obtained, and the standard deviation is calculated from thermal anomalies of these 200 samples.

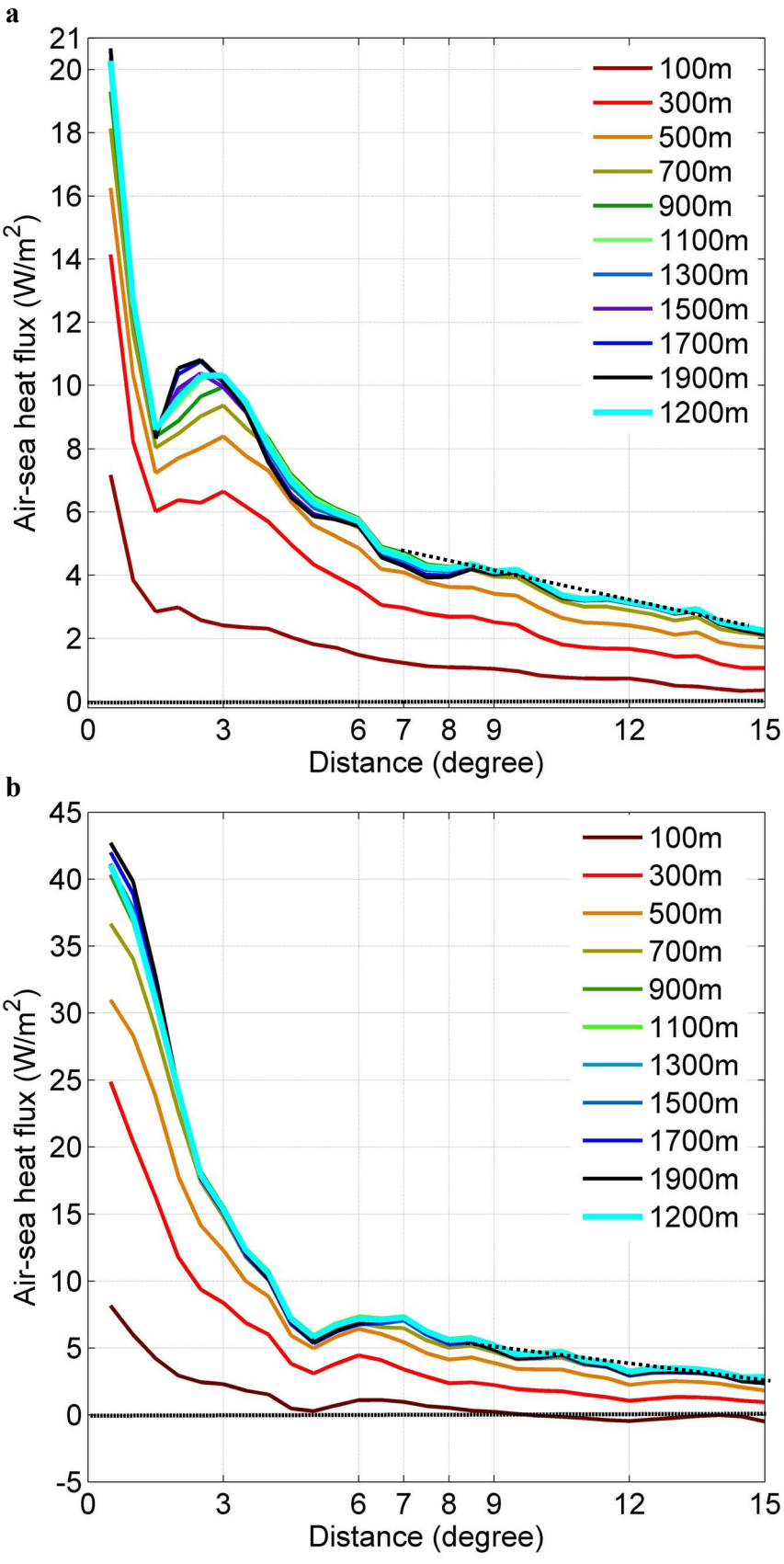

Figure 7. Estimates of air-sea heat flux within TC with different footprint domain sizes (horizontal and depth) for: a) TS/TDs and b) Hurricanes. The results of 1200m are highlighted in cyan.

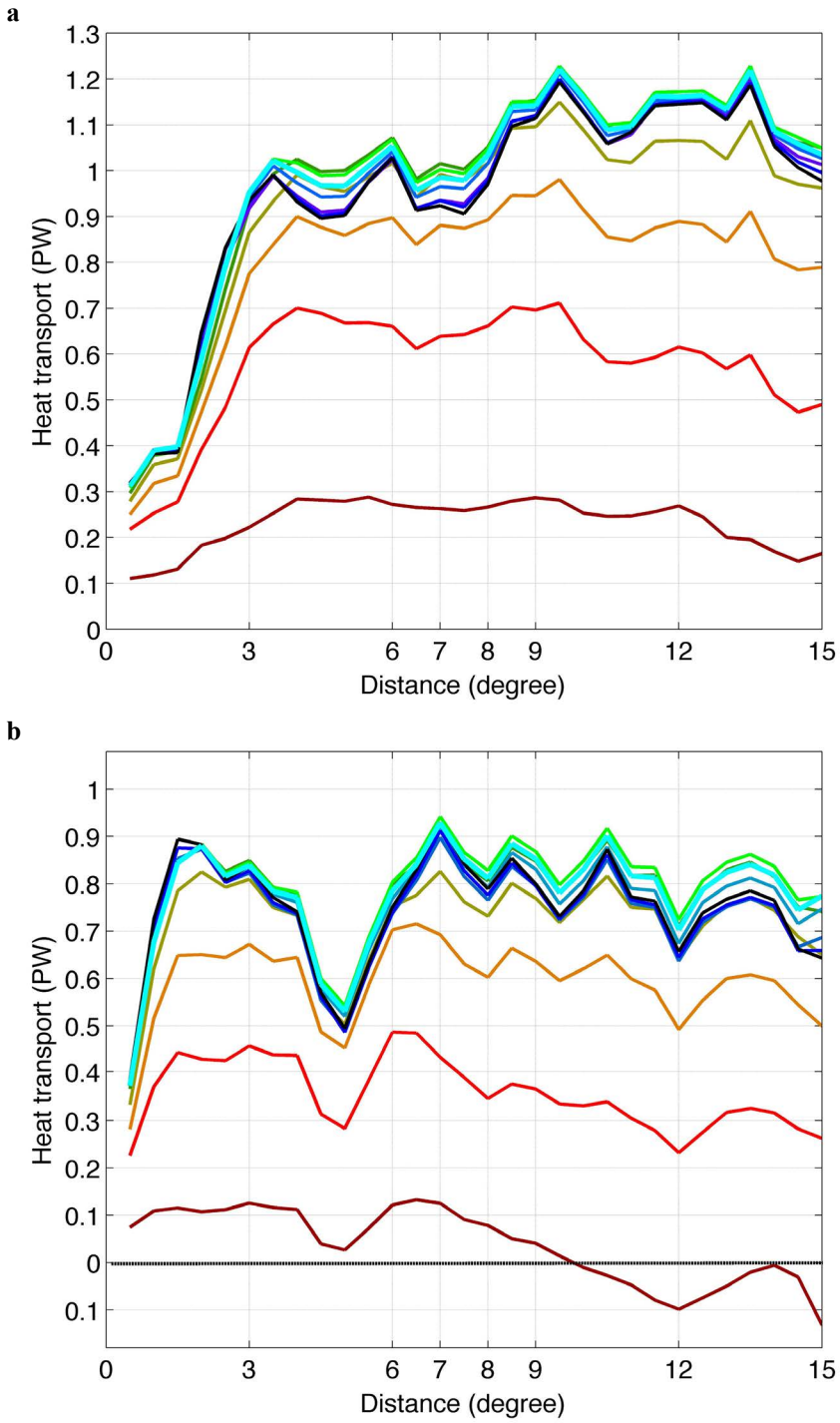

Figure 8. The impacts of domain size on global annual heat transfer from the ocean to the atmosphere by TCs for: a) TS/TDs and b) Hurricanes. The colors are the same to those in Figure 7.

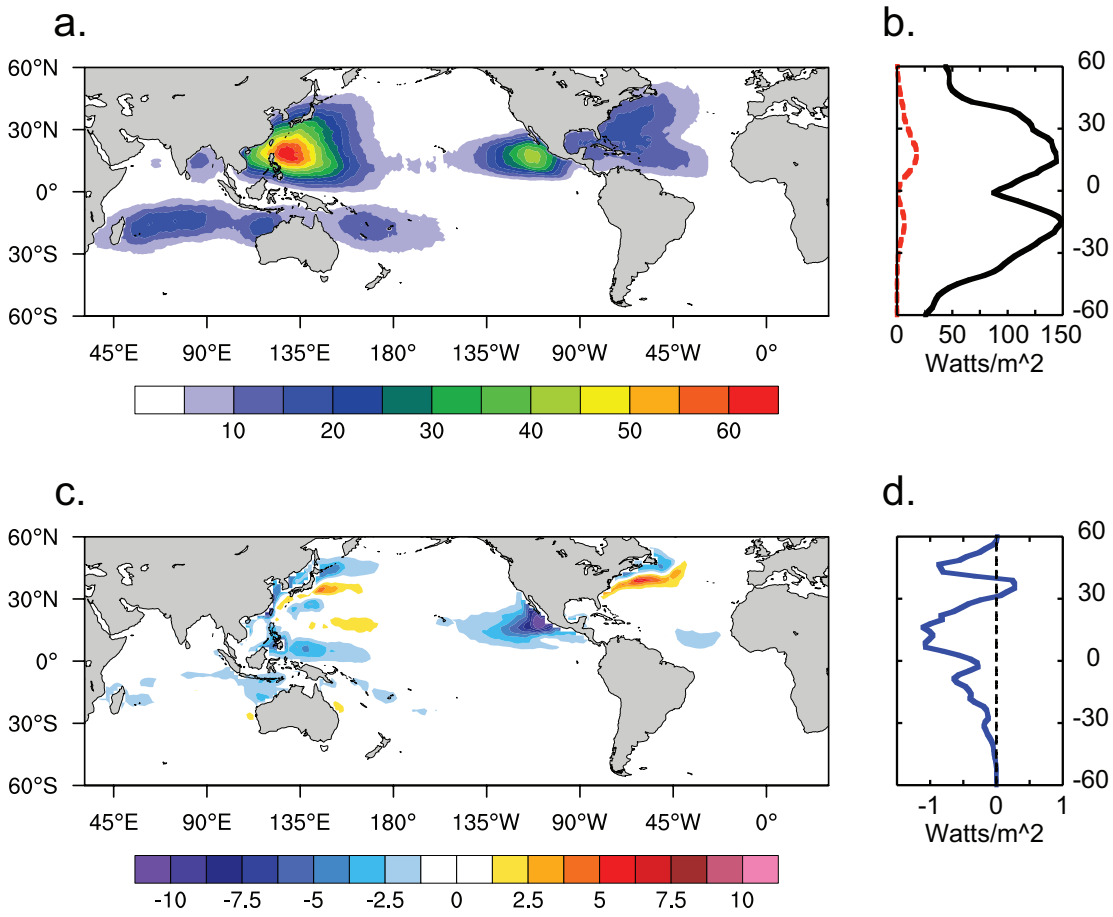

Figure 9. Geographical pattern of air-sea heat flux caused by TCs. a) Globally integrated net heat flux caused by TCs calculated using Argo float data (W/m^2). b) Zonally averaged TC-induced heat flux (red curve), compared with the annual climatology (1990-2010) of air-sea latent heat flux (black curve) derived from NCEP/NCAR reanalysis (Kalnay et al. 1996). c) Net surface flux (positive upward) along storm tracks for climatological conditions during the period 1990-2010 (W/m^2), derived from NCEP/NCAR reanalysis using storm tracks from 1990-2010. The plot represents the background air-sea flux contribution to the Argo analysis using the 20-year daily climatology. d) Zonal average of the climatological net surface heat fluxes shown in c.

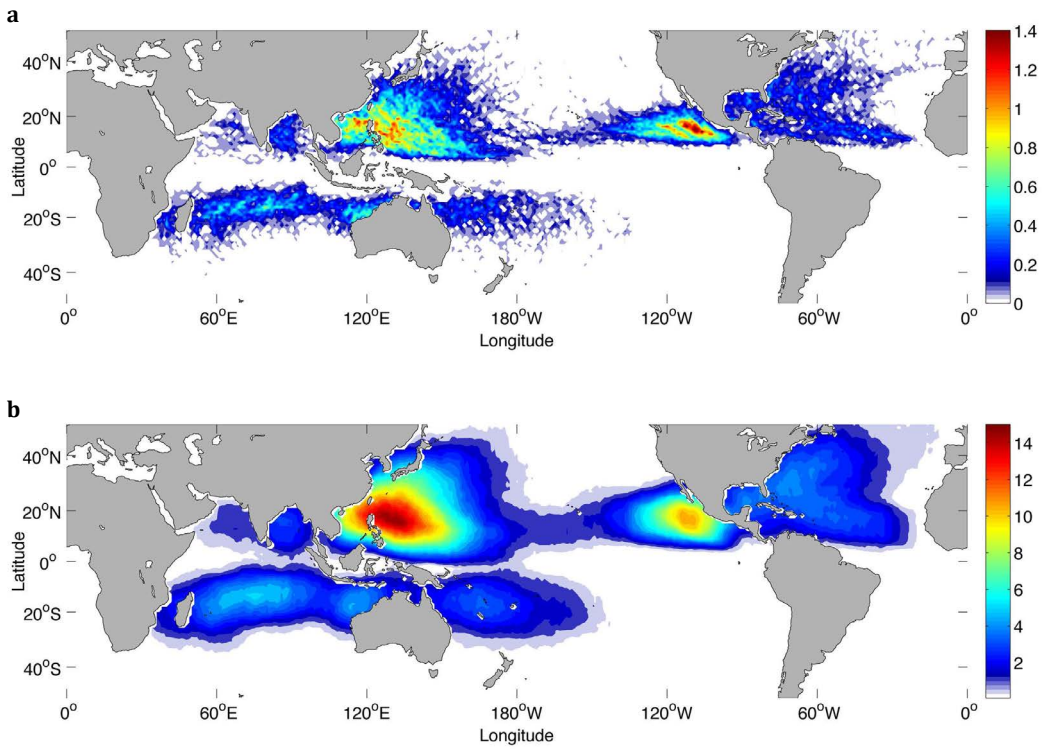

Figure 10. Frequencies of tropical cyclones per year affecting 1^{o} by 1^{o} grid boxes, when the TC-affected region is assumed to be a) ±1 degree from the track center, and b) ±8 degrees from the track center.

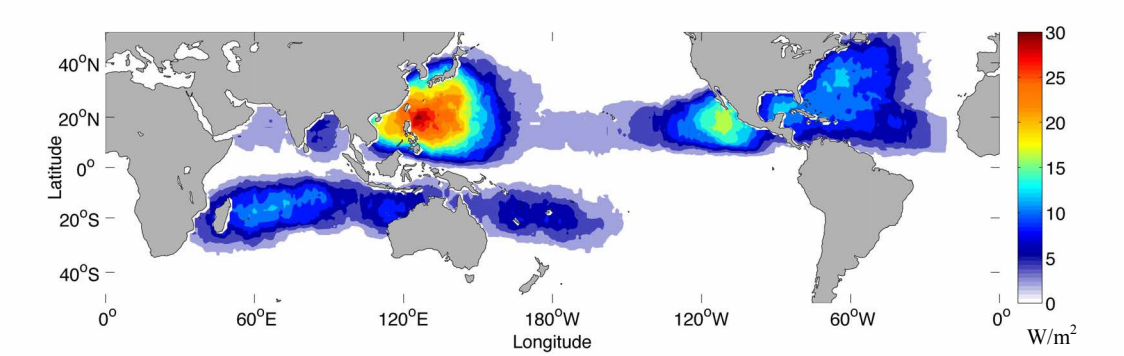

Figure 11. Geographical distribution of air-sea heat flux caused by TCs. We assume each grid box can only be affected by 1 storm within a 20 day window.

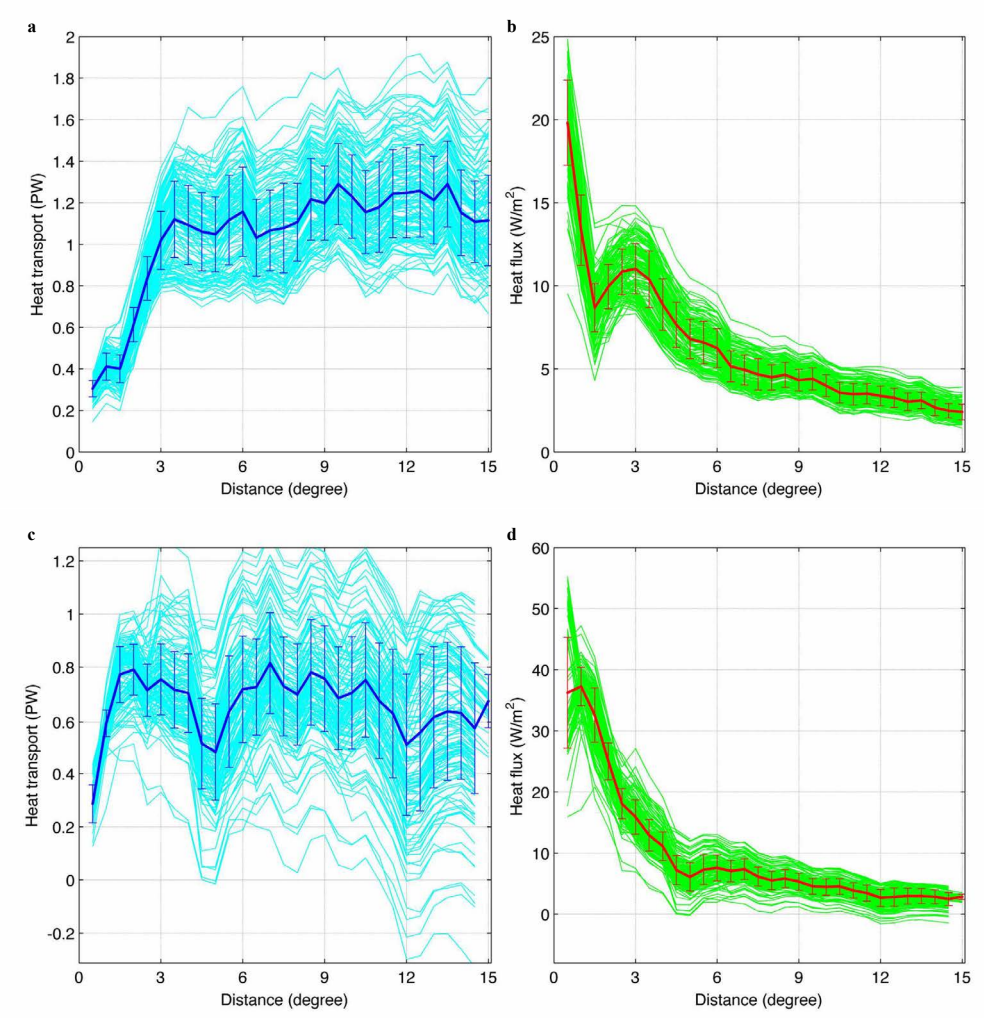

Figure 12. 200 estimates on heat transport (in a) and c)) and air-sea heat flux (in b) and d)) based on 200 randomly selected samples of pairs. a) and b) are estimates under TS/TD conditions and b) and c) for hurricanes. The mean of 200 estimates is highlighted in blue for TS/TD and in red for hurricane. Error bars represent the standard error.

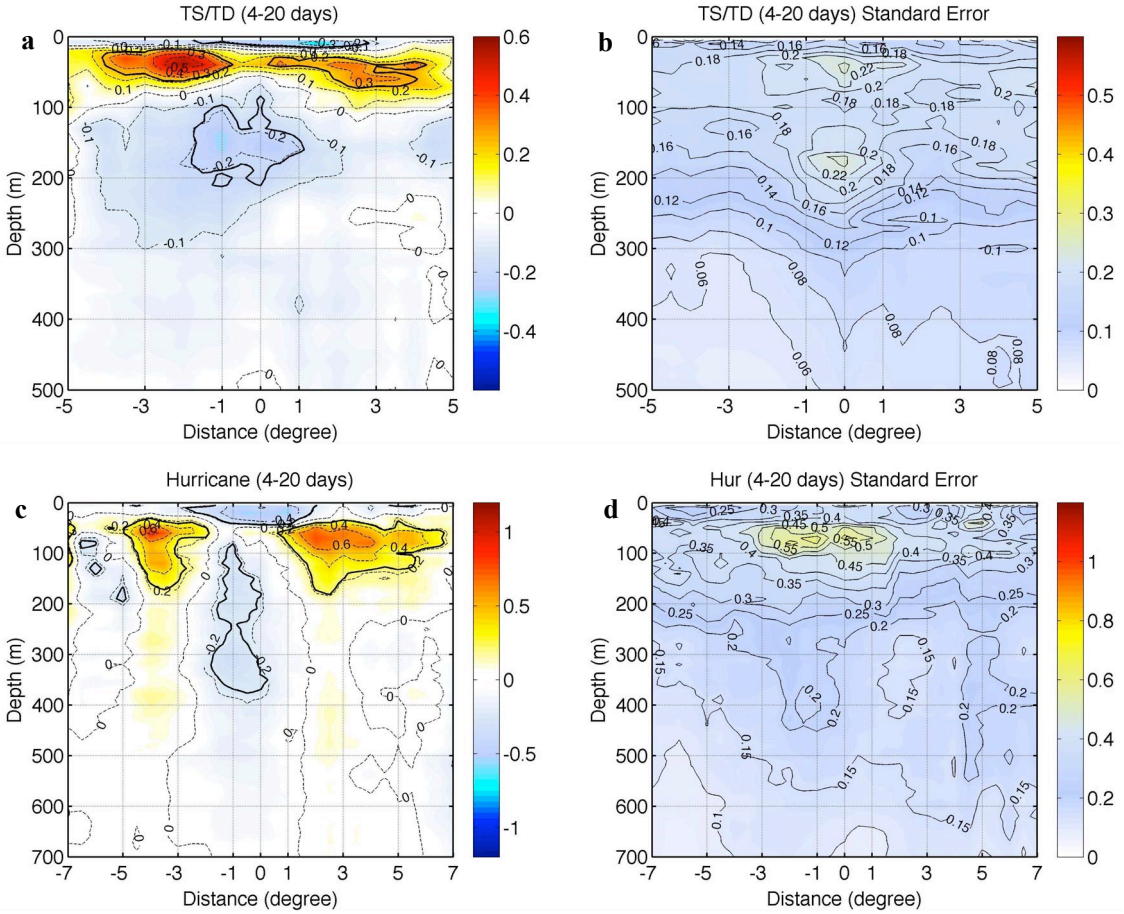

Figure 13. Vertical profile of the 4-20 days averaged ocean thermal changes (referenced to pre-storm conditions) from the track center for: a) TS/TD between +5 and - 5 degrees and c) Hurricanes between +7 and - 7 degrees. The dashed contours interval in black is 0.1°C for TS/TD and 0.2°C for Hurricane. The solid black contours denote the signals that are significant at 90% confidence interval. b) and d) shows the standard error of the estimations corresponding to a) and c) respectively. The unit is °C.

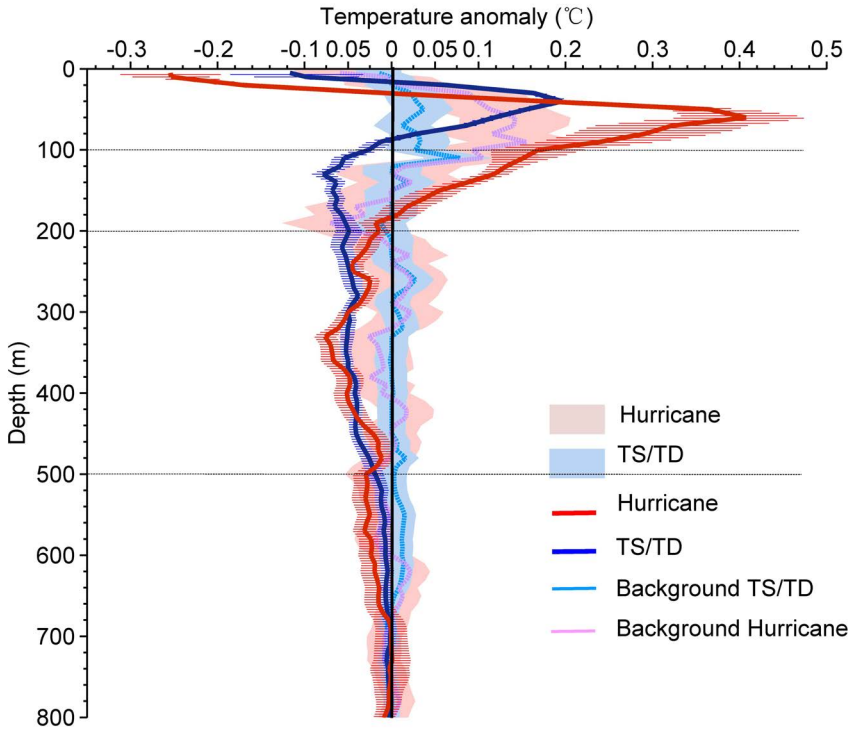

Figure 14. Vertical temperature change averaged within the -6 to +6 degree range from storm center during the recovery stage (4-20 days) relative to pre-storm conditions. Blue and red lines represent TS/TD and Hurricanes, respectively. Also plotted are the 90% confidence intervals in Null-hypothesis test (light blue and light pink shading for TS/TD and hurricane, respectively). The light blue and pink curves show the mean background noise in TS/TD and Hurricane subsets respectively. The error bars represent the standard deviations, which are calculated by using the method as presented in Figure 6.

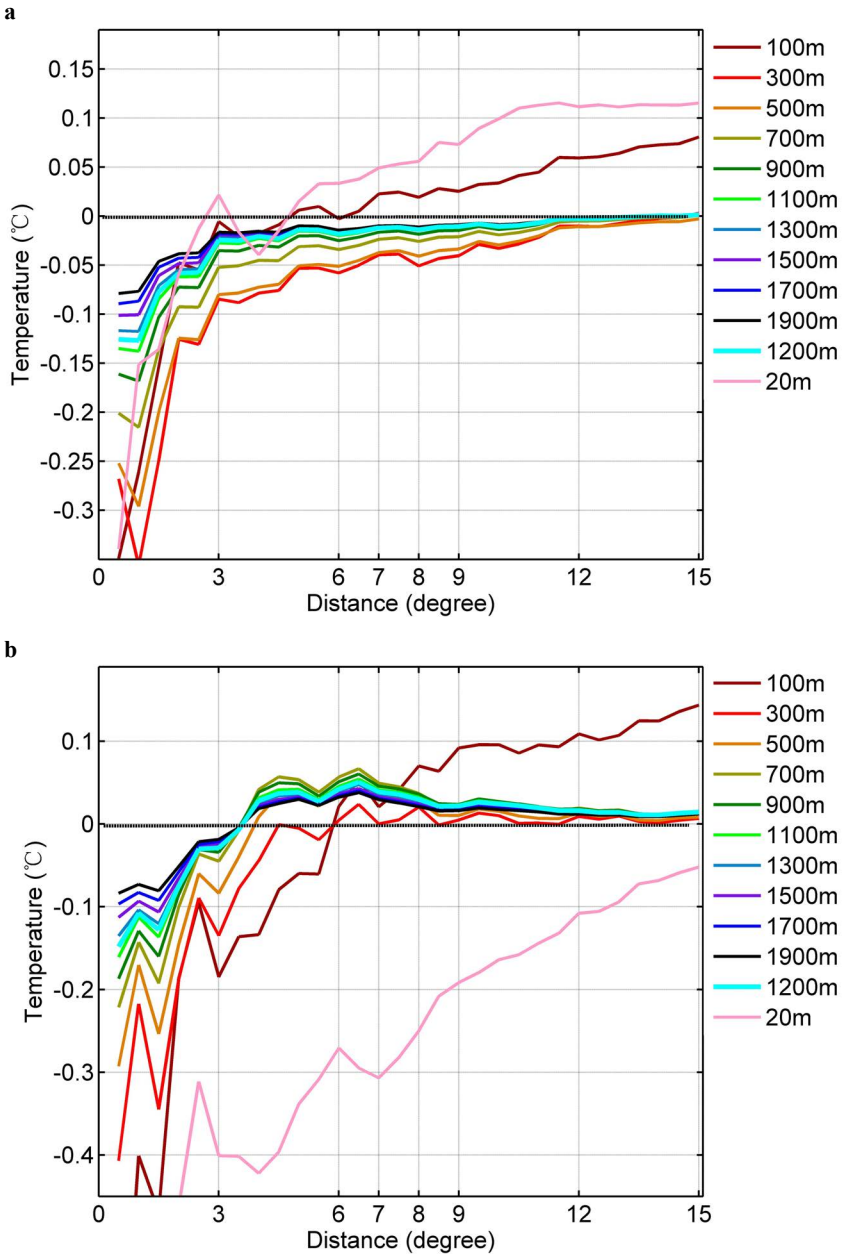

Figure 15. Column averaged temperature anomalies within 4-20 days after tropical cyclones, relative to pre-storm conditions, as a function of the horizontal box size across the storm track (from ±1 degree to ±15 degree) for: a) TS/TD, and b) hurricanes. The colors are different vertical size of the TC-affected box from 100m to 1900m. The results for the box with 1200m depth is highlighted in cyan.

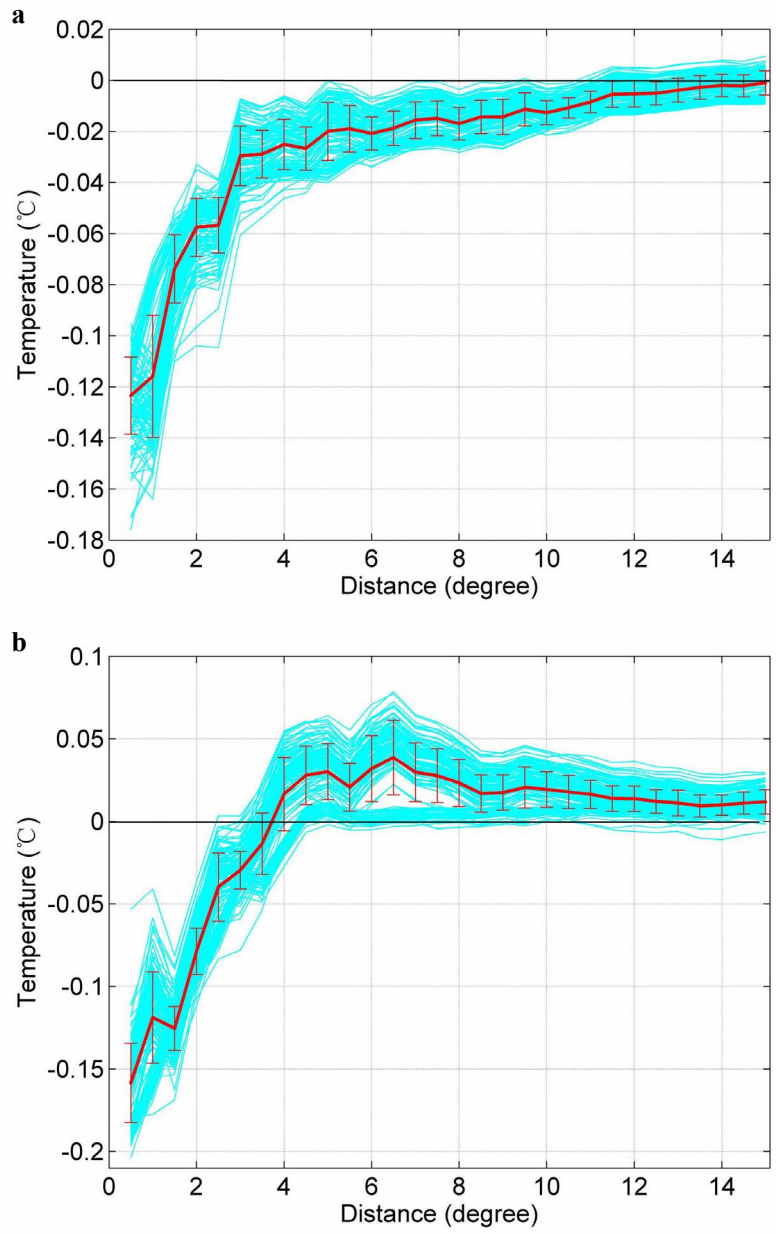

Figure 16. 200 estimates (in cyan) of 0-1200m column averaged temperature as a function of distance across the storm track, based on randomly sampling 90% of the Argo pairs for: a) TS/TD and b) Hurricanes respectively. The mean and standard deviations are highlighted as the red line and error bars.

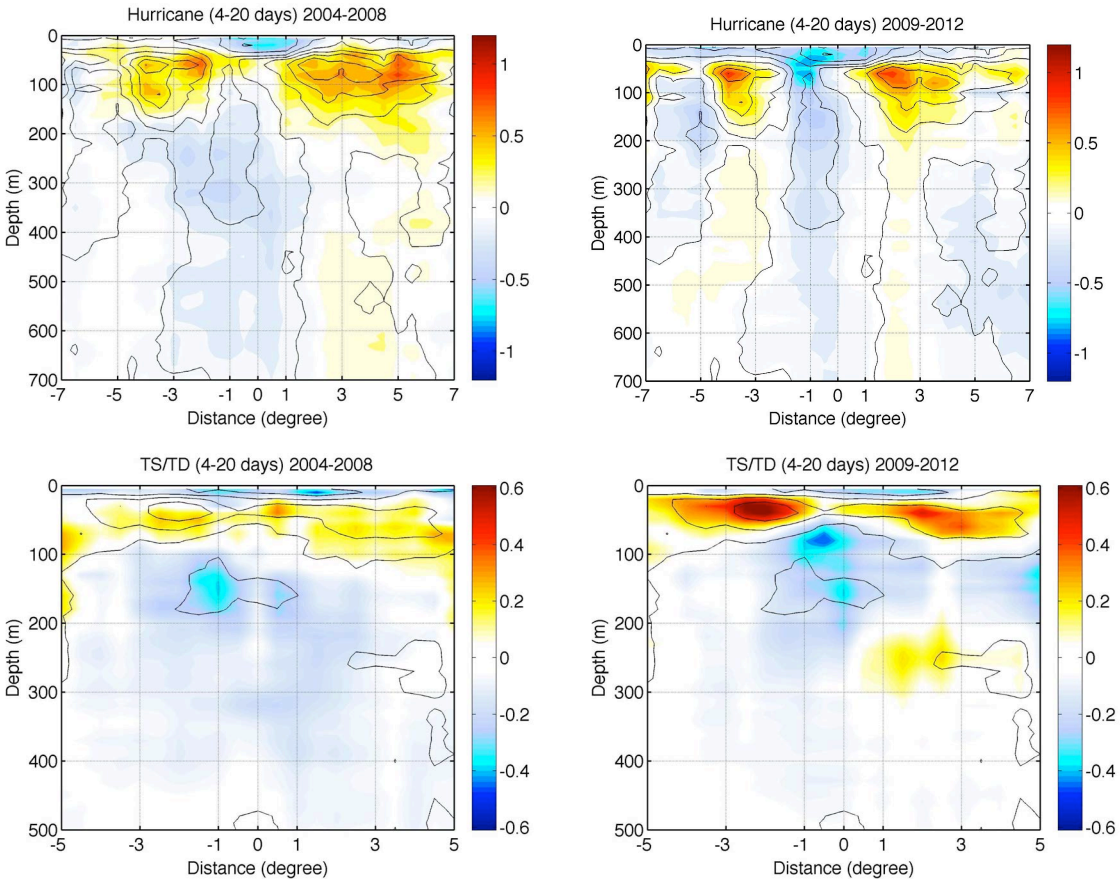

Figure 17. The 4-20 days averaged ocean thermal changes detected by using data from two year periods: 2004-2008 in the left panel and 2009-2012 in the right panel, shown in colors. The black contours are the result when using all of the data from 2004 to 2012, the same to the contours in Figure 13. The results of Hurricane are presented in the top panel and the bottom panel for TS/TD. The unit is ^{o}C.

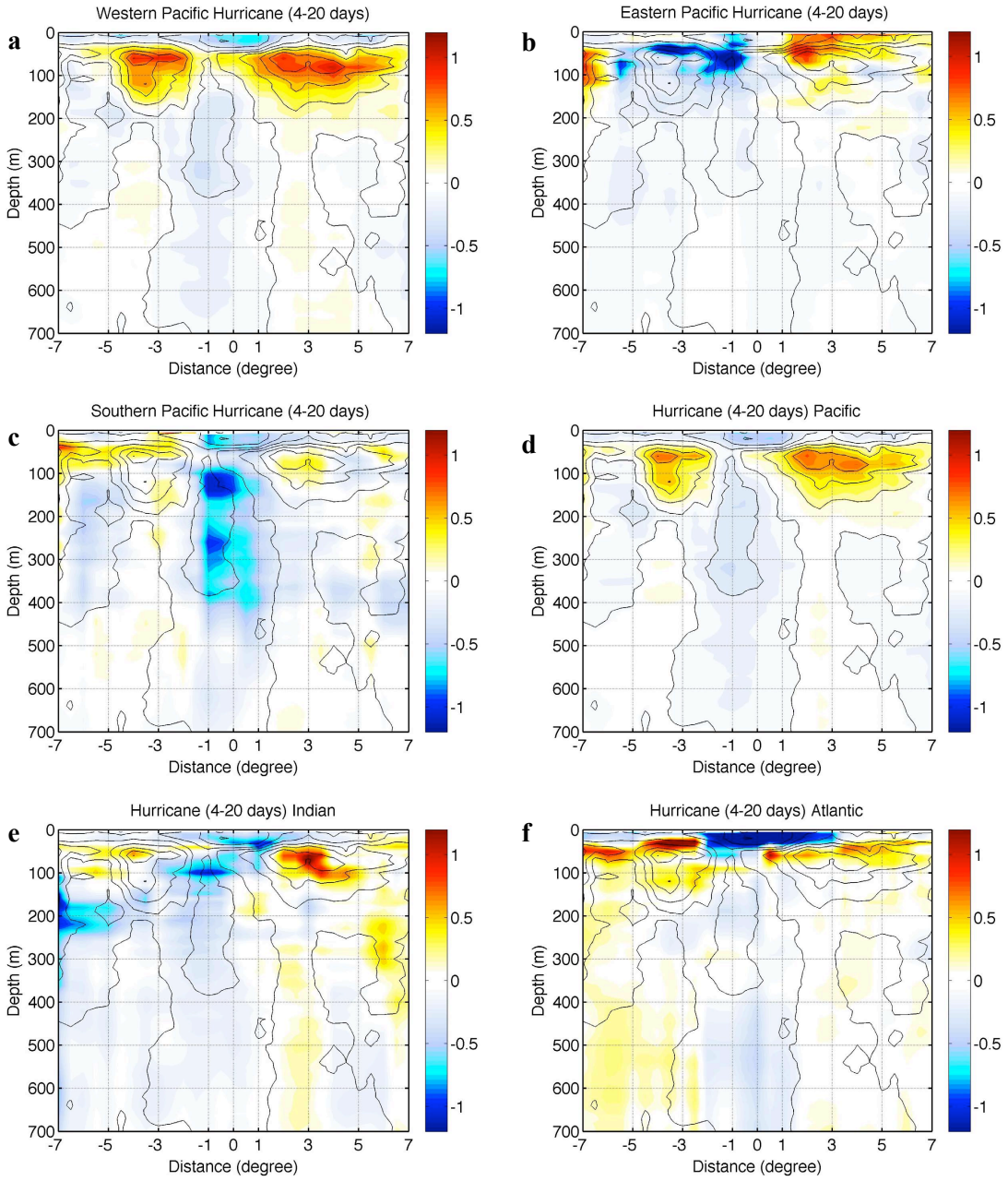

Figure 18. Ocean thermal changes induced by hurricanes within 4-20 days after storm passage for individual ocean basins: a. in Western Pacific Ocean, b. in Eastern Pacific Ocean, c. in Southern Pacific Ocean, d. in Pacific Ocean, e. in Indian Ocean, f. in Atlantic Ocean. The black contour is the global-averaged hurricane-induced ocean thermal changes in 4-20 days, which is the same to that in Figure 13c. The unit is ^{o}C.

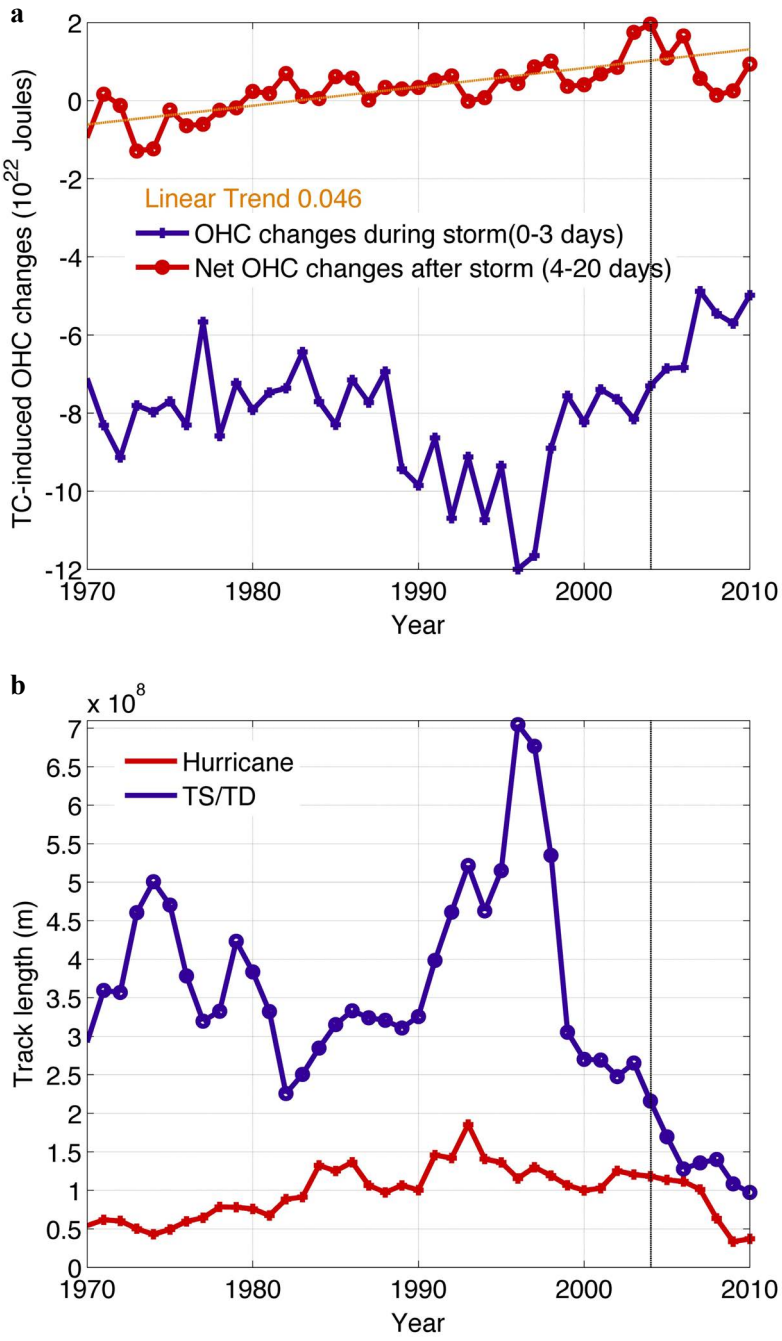

Figure 19. a): The annual TC-induced ocean heat loss via air-sea heat flux in 0-3 days (blue line) and the net ocean heat content changes after storm (in 4-20 days) (red line). The positive values show the net heat gain. The linear trend of the net ocean heat gain is presented in pink, and the trend is 0.046×10^{22} J/year. b): Yearly averaged track lengths for both TS/TD (blue) and hurricanes (in red).

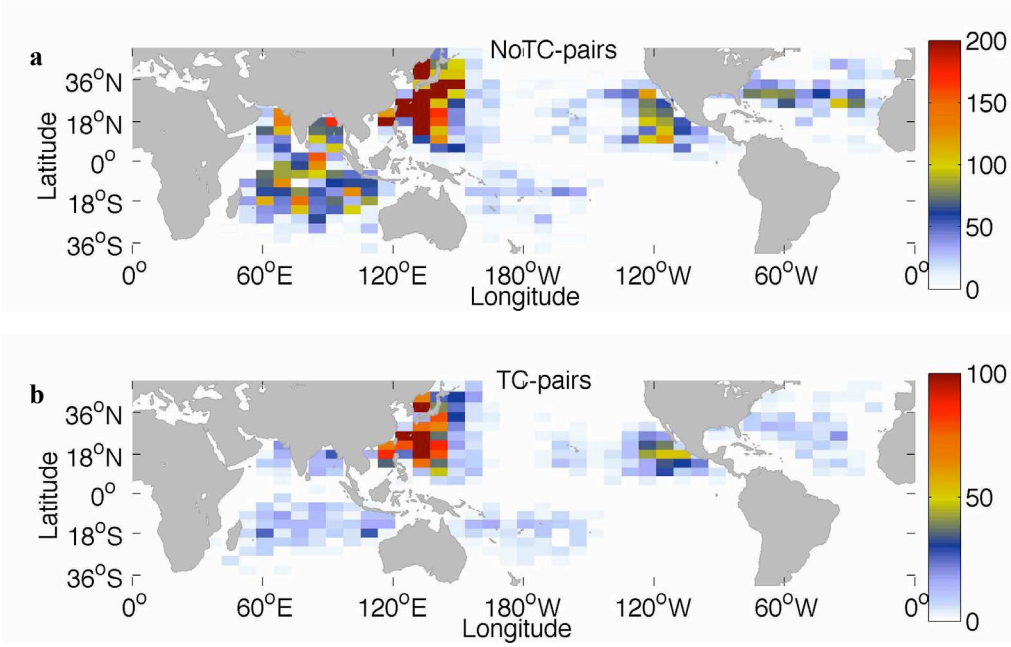

1

2 Figure A1. Counts of the a) NoTC-pairs and c) TC-affected pairs in each 4° by 8°

3 degree grid box.

4

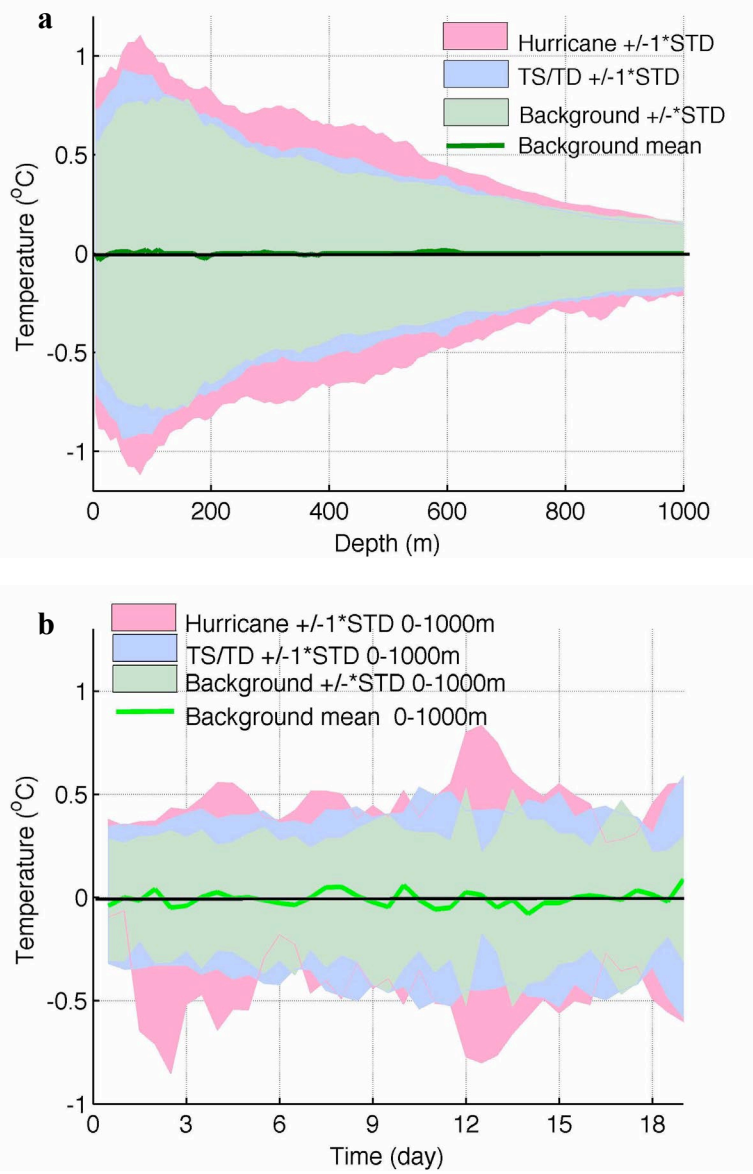

Figure A2. Background ocean temperature variability as a function of depth and time. a) Mean (green curve) and one standard deviation (green shading) of background variability as a function of depth, compared with one standard deviation of hurricane and TS/TD affected pairs. b) Time evolution of background variability of 0-1000m average (light green line and light green shading for mean and standard deviation respectively). The standard deviations of temperature anomalies in Argo pairs under TS/TD and hurricane conditions are plotted in light blue and light red, respectively.

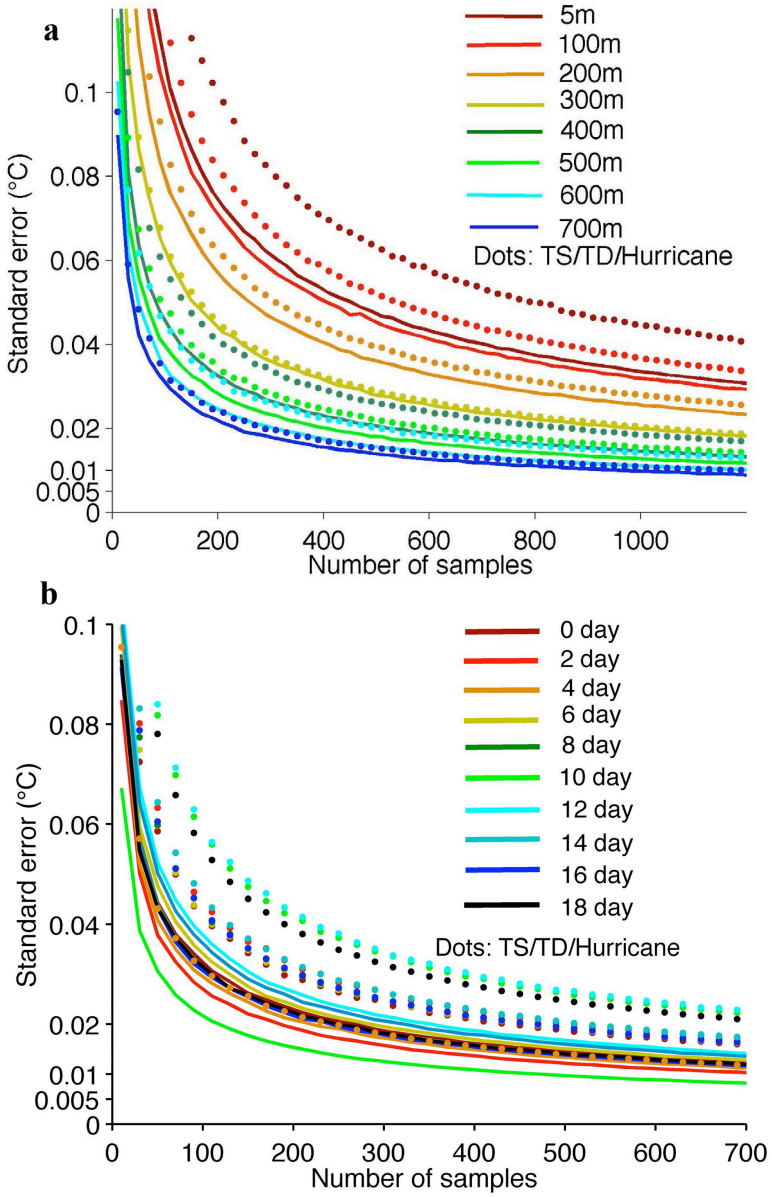

Figure A3. Bootstrap analyses of background noise. a) Standard errors at different depth versus sample numbers with colors denoting different depths. b) Standard errors at different times versus sample numbers with colors denoting different time. Solid lines are the results by using the whole NoTC-pairs dataset, and the dots show the same results for the TC-affected pairs.

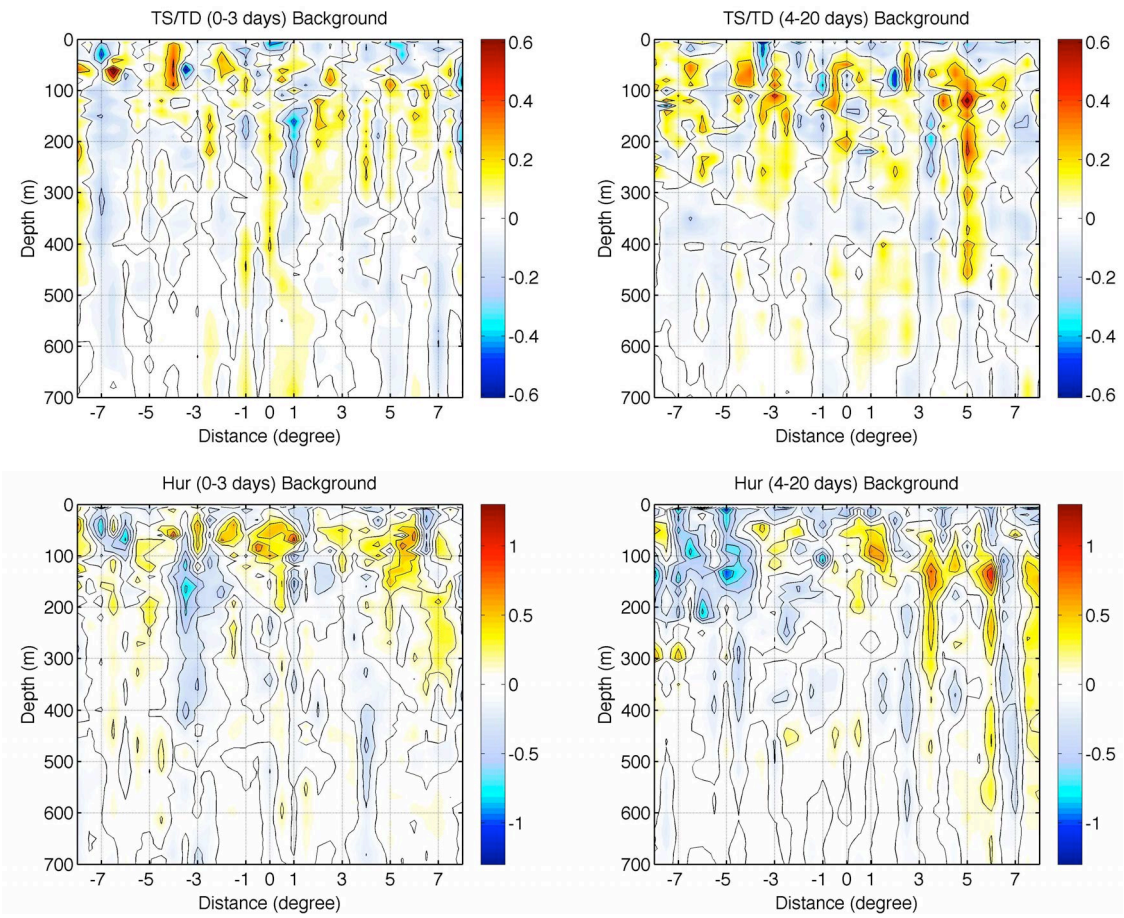

Figure A4. Background ocean thermal changes as a function of depth and distance in TC track coordinates. The background footprint is created corresponding to TS/TD footprint a) on 0-3 days average and b) on 4-20 days average, and to Hurricane footprint c) on 0-3 days average and d) on 4-20 days average. The contours interval is 0.2°C in black. The units are °C.

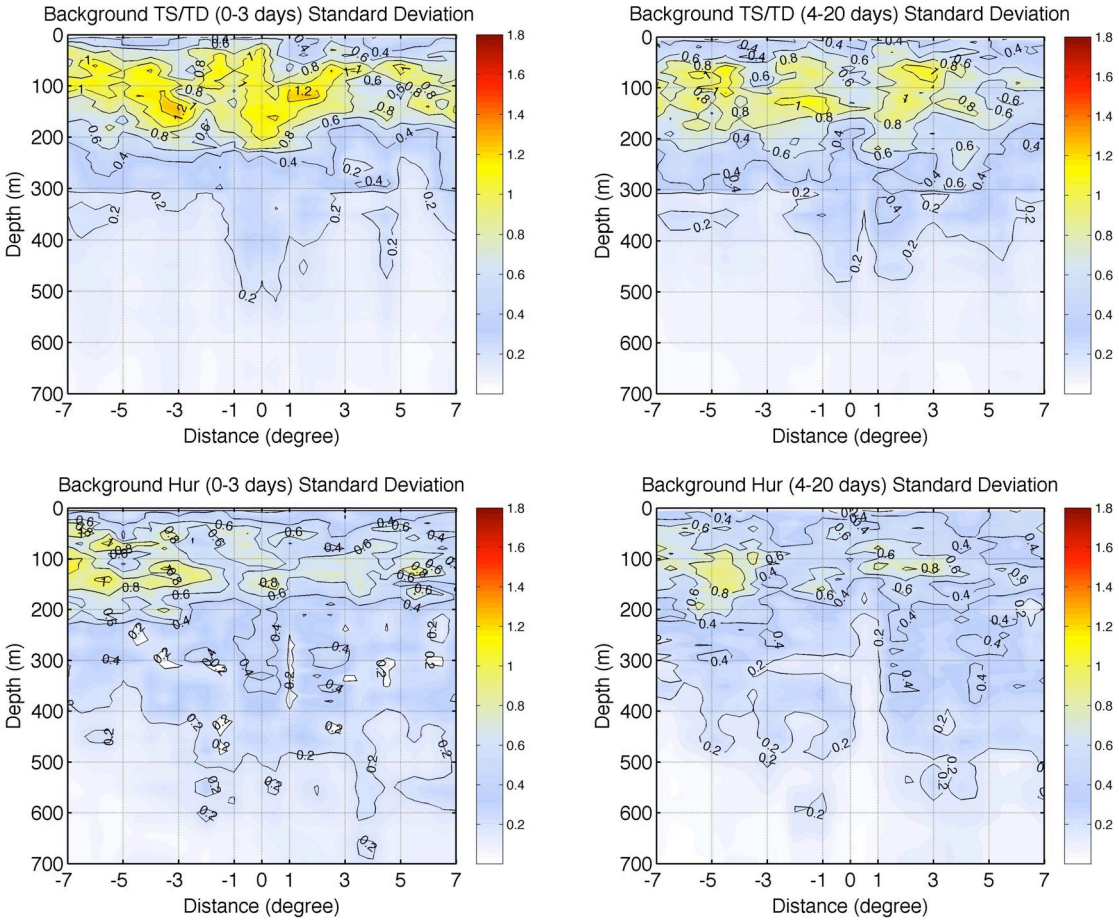

Figure A5. Standard deviation of the background footprints for TS/TD and Hurricane locations respectively on two time periods: 0-3 days and 4-20 days. The unit is ^{o}C.

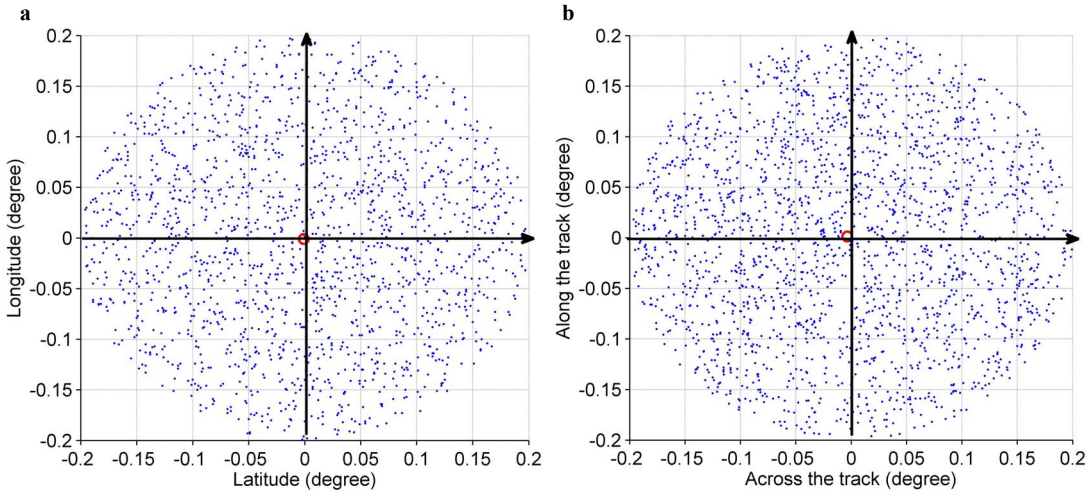

Figure A6. Schematic scatter plots showing Argo floats drifting destination from the origin. Two coordinate systems are: a) latitude-longitude, with the location of the float before storm as origin; b) Track direction as y-axis, and the location of the float before the storm as the origin. The red dots are the destination of the pairs with pairs from the same float in red (with the mean in red star) pairs from different floats in blue (with the mean in big blue dot).

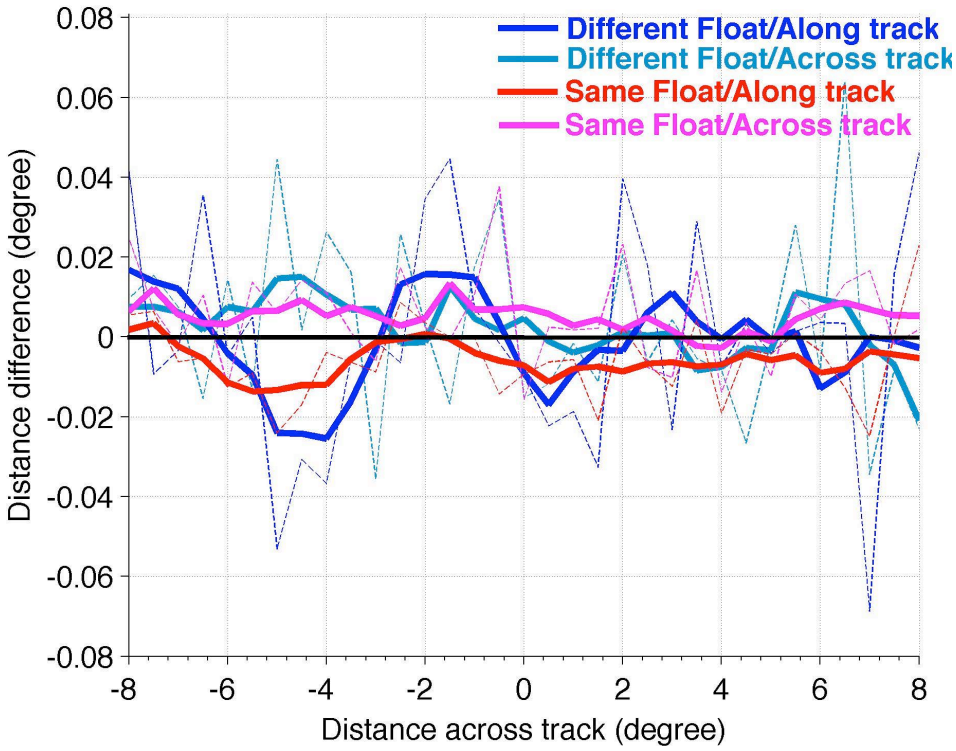

Figure A7. Horizontal distance difference between the two profiles in a TC-affected pair along and across the track as a function of the distance from the float location to the track center. Here the distance is calculated in track coordinates, i.e: positive distance across the track represents the inertial-resonant side (right side in Northern hemisphere and left side in Southern hemisphere). The horizontal distances by using pairs that the two profiles are from different floats are shown in dark blue (along track) and light blue (across track), while drifting distances based on the remaining pairs are shown in purple (across track) and red (along track).